ABSTRACT

Compressibility Effects on Rotor Forces in the Leakage Path between a Shrouded
Pump Impeller and Its Housing. (August 1993)
Nhai The Cao, B.S., Texas A&M University
Chair of Advisory Committee: Dr. Dara Childs

A modified approach to Childs' previous work (1989,1992) on fluid-structure interaction forces in the leakage path between an impeller shroud and its housing is presented in this paper. Three governing equations consisting of continuity, path-momentum, and circumferential-momentum equations were developed to describe the leakage path inside a pump impeller. Radial displacement perturbations were used to solve for radial and circumferential force coefficients. In addition, impeller-discharge pressure disturbances were used to obtain pressure oscillation responses due to precessing impeller pressure wave pattern. Childs' model was modified from an incompressible model to a compressible barotropic-fluid model (the density of the working fluid is a function of the pressure and a constant temperature only). Results obtained from this model yielded interaction forces for radial and circumferential force coefficients. Radial and circumferential forces define reaction forces within the impeller leakage path.

An acoustic model for the same leakage path was also developed. The convective, Coriolis, and centrifugal acceleration terms are removed from the compressible model to obtain the acoustics model. The compressible model is compared with the incompressible model and the acoustic model. A solution due to impeller discharge pressure disturbances model was also developed for the compressible and acoustic models. The results from these modifications are used to determine what effects additional perturbation terms in the compressible model have on the acoustic model.

The results show that the additional fluid mechanics terms in the compressible

model cause resonances (peaks) in the force coefficient response curves. However, these peaks only occurred at high values of inlet circumferential velocity ratios, $u_{\theta 0}(0) > 0.7$. The peak pressure oscillation was shown to occur at the wearing ring seal. Introduction of impeller discharge disturbances with $n = 11$ diametral nodes showed that maximum peak pressure oscillations occurred at nondimensional precession frequencies ($f = \Omega/\omega$ where ω is the running speed of the pump) of $f = 6.4$ and $f = 7.8$ for this particular pump. Bolleter's results suggest that for peak pressure oscillations to occur at the wearing ring seal, the nondimensional excitation frequency should be on the order of $f = 2.182$ for $n = 11$. The resonances found in this research do not match the excitation frequencies predicted by Bolleter. At the predicted peak excitation frequencies given by Bolleter, the compressible model shows an attenuation of the pressure oscillations at the seal exit.

The compressibility of the fluid does not have a significant influence on the model at low values of nondimensional excitation frequency. At high values of nondimensional frequency, the effects of compressibility become more significant. For the acoustic analysis, the convective, Coriolis, and centrifugal acceleration terms do affect the results to a limited extent for precession excitation and to a large extent for a pressure excitation when the fluid operates at relatively high Mach numbers.

To the memory of my grandfather, Cao Van Tac.

.

ACKNOWLEDGEMENTS

TABLE OF CONTENTS

LIST OF FIGURES

LIST OF TABLES

NOMENCLATURE

A_{1s}, A_{2s}, A_{3s}, A_{4s}, $A_{1\theta}$, $A_{2\theta}$,

$A_{3\theta}$, $A_{4\theta}$ coefficients introduced in Eq. (32-33)

$b = V_i/R\omega$ nondimensional velocity ratio

C_{dc} discharge coefficient for the exit wearing ring seal (Eq. 11)

C_i initial (s=0) clearance (L)

C_r exit (s=1) clearance (L)

$f = \Omega/\omega$ nondimensional frequency ratio

$h = H/C_i$ nondimensionalized clearance

H clearance between impeller shroud and housing (L)

L path length (L)

L_s leakage path length (L)

M Mach number - fluid velocity/acoustic velocity

n difference in number of impeller blades and diffuser vanes

P fluid static pressure (F/L^2)

$p = P/\rho V_i^2$ dimensionless pressure

$p_s(\theta,t)$ dimensionless inlet supply pressure (s=0)

$p_e(\theta,t)$ dimensionless exit pressure (seal exit)

R radial coordinate (L)

R_i initial radial coordinate (s=0)

$R_\alpha = 2HU_s/\nu$ Reynolds number defined in Equation (8)

$r = R/R_i$ nondimensionalized radial coordinate

S Path coordinate (L)

$s = S/L_s$ nondimensionalized path length

$T = L_s/V_i$ representative transit time for fluid traversing the leakage path (T)

t Time (T)

$u_s = U_s/V_i$ nondimensionalized path fluid velocity

$u_\theta = U_\theta/R_i\omega$	nondimensionalized circumferential fluid velocity
U_s, U_θ	path and circumferential velocity of fluid (L/T)
V_i	initial (s=0) path fluid velocity
ϵ	perturbation parameter
λ_r, λ_s	Friction factor definitions defined in Eq. (19)
σ_r, σ_s	Wall friction factor defined in Eq. (19)
μ	Fluid viscosity (F-T/L^2)
ρ	Fluid density (m/L^3)
$\bar{\rho} = \rho/\rho_i$	nondimensionalized fluid density
$\tau = \omega t$	nondimensionalized time
τ_w	Wall shear stress (F/L^2)
τ_s, τ_r	Shear stress on stator and rotor surfaces (F/L^2)
θ	Circumferential coordinate
ω	Rotor angular velocity (T^{-1})
Ω	Shaft whirl angular velocity (T^{-1})
ξ	Inlet loss coefficient
ν	Kinematic viscosity (L^{2}T^{-1})

Subscripts

r, s	Rotor and stator
z, θ	Axial and circumferential directions
0, 1	Zeroth and first-order perturbations

CHAPTER I

INTRODUCTION

In the past, wear-ring seals used on the SSME HPFTP (Space Shuttle Main Engine High Pressure Fuel Turbopump) made from KEL-F plastic came back after operation revealing highly unusual characteristics. Despite being in constant contact with liquid hydrogen, post-test inspection showed that interior points in the stator element had melted and resolidified. The material used in the seal stator has poor heat conduction properties and high internal hysteretic damping. Pressure oscillations adjacent to the seal may be a source of cyclic stress producing hysteretic losses. This investigation will examine the pressure oscillations which may cause cyclic stresses in the leakage path between the impeller shroud and its housing. Possible sources of excitation causing the seal to melt and resolidify will be investigated.

For this project, an analysis will be performed for a bulk flow model of the leakage path between a pump impeller shroud and a housing along the front side of the impeller, from inlet to discharge (Fig. 1). Simply defined, a bulk flow model considers only the average of the velocity distribution across the flow field. The research will be an extension of analyses performed previously by Childs (1989, 1992) for a shrouded pump impeller and its housing.

The working fluid will be modelled as a barotropic fluid in this analysis, instead of an incompressible fluid, to account for fluid compressibility. The density and viscosity of barotropic fluids depend only on the local pressure and are independent of temperature. This assumption is reasonable for most cryogenic fluids, where viscosity is low and effects of viscous heating are negligible. The properties of the working fluid, i.e., density and viscosity, will be implemented into a new analysis by using a general 32-term, thermodynamic, equations-of-state program, MIPROPS (McCarty, 1986, modified by San Andres, 1991).

This paper is modelled after the ASME *Journal of Tribology*.
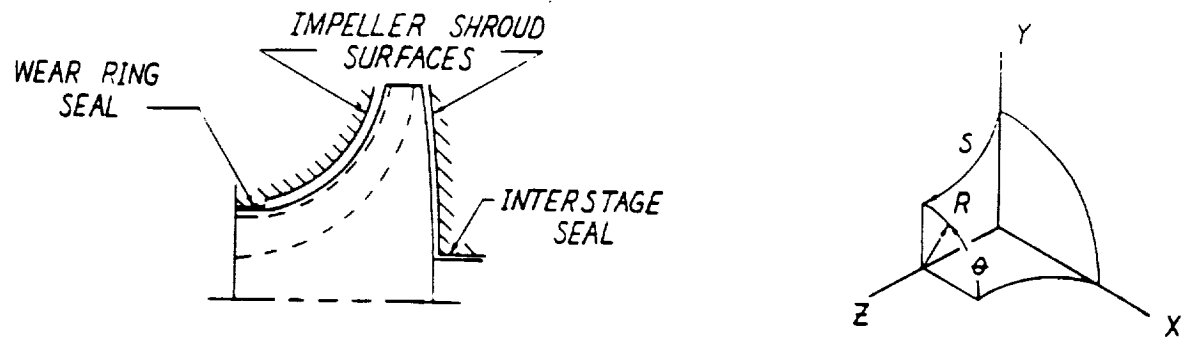
Figure 1 - Impeller stage and surface geometry

CHAPTER II
LITERATURE REVIEW

Childs (1989) performed a bulk-flow analysis for the leakage path between an impeller shroud and a pump housing. Three governing equations of motion were derived for a bulk-flow model to represent incompressible fluid flow in the leakage path of a conventional water pump impeller. Three equations, consisting of a continuity equation, a path-momentum equation, and a circumferential-momentum equation, were used to solve for rotordynamic forces due to a precessional excitation of the rotor.

Childs used a perturbation expansion in the eccentricity ratio of the governing equations of fluid motion for small motions about a centered impeller position yielding a set of zeroth and first-order governing equations. A zeroth-order solution was obtained by an iterative procedure to define the leakage, pressure, and circumferential-velocity distribution. Using a perturbed clearance function due to a radial displacement perturbation, Childs evaluated the first-order model at several inlet circumferential velocity conditions to obtain the first-order perturbed solutions. First-order perturbation results provided rotordynamic coefficients (direct and cross-coupled stiffness, damping, and mass) and lateral reaction forces for the model. Childs' predictions for the impeller of Fig. 2 are shown in Fig. 3. The predicted radial and circumferential force coefficients are shown versus the nondimensional precessional frequency for nondimensionalized inlet circumferential velocities of $u_{\theta 0}(0) = 0.5, 0.6$, and 0.7. Nondimensional precessional frequency is the ratio of the impeller precession frequency, Ω, to its running speed, ω. The graphs showed a considerable "dip", or resonance, in the radial and circumferential force response coefficients at higher values of $u_{\theta 0}(0)$. The radial and circumferential force coefficients represent the nondimensionalized reaction forces acting on the impeller face due to impeller precession. Childs showed that the centrifugal acceleration terms in the momentum equations produced the "dip" in the results. By removing the
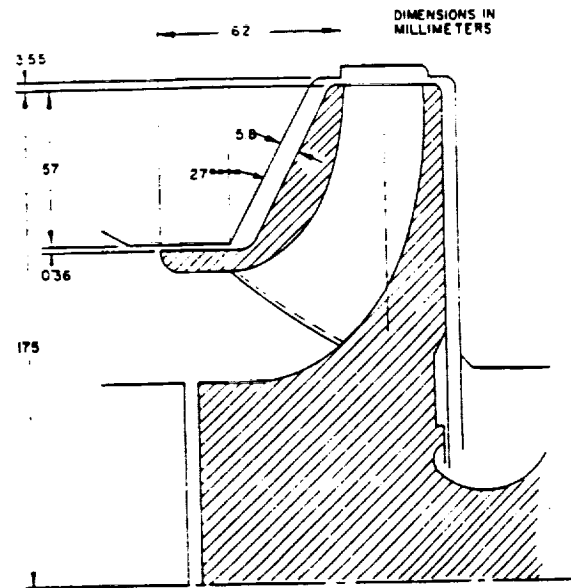
Figure 2 - Nominal configuration of conventional water impeller
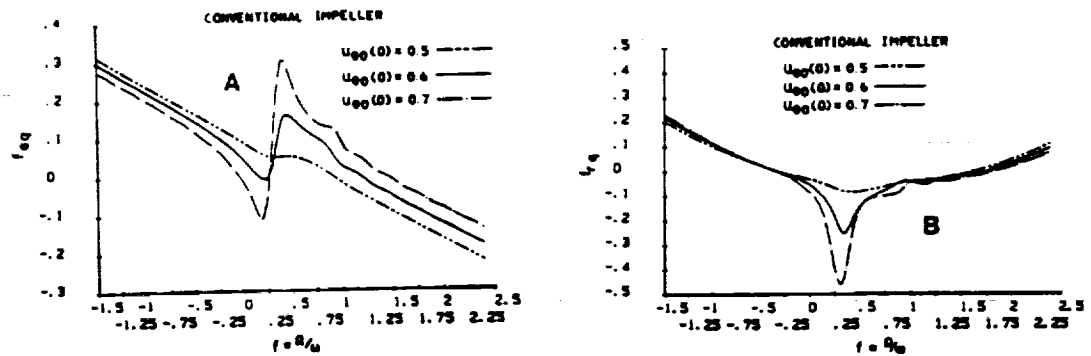
Figure 3 - Nondimensional force coefficients for the conventional impeller (a) circumferential-force coefficient, (b) radial-force coefficient

centrifugal acceleration term from the path-momentum equation, the "dips" in the plots were eliminated.

Bolleter (1988) presents a relationship between the difference (n) in the number of impeller blades (n_1) and diffuser vanes (n_2) and the precessional frequency for pressure pulsations in an impeller leakage path. Various combinations of impeller blade and diffuser vane number causing vibrations and pressure pulsations in the impeller are described. The relationship presented by Bolleter states that a pressure pattern develops with $n = |n_1 - n_2|$ diametral nodes around the impeller exit. The precession velocity of the pressure oscillation is $n\omega_1/(|n_1 - n_2|)$. For example, an impeller with $n_1 = 11$ blades and $n_2 = 6$ diffuser vanes would have amplifications of the pressure oscillations at frequencies of multiples of $11\omega/(|11 - 6|) = 2.2\omega$.

Childs (1992) performed an analysis similar to (Childs, 1989) incorporating the effects of different numbers of impeller blades and diffuser vanes for the bulk flow model using excitations due to discharge-pressure oscillations instead of orbital motion. This analysis considered the harmonic response of flow within the annulus due to variations in the discharge pressure of the impeller. This analysis also compared the effect on the response of the pressure oscillation due to different numbers of pump impeller blades and diffuser vanes. Zeroth and first-order perturbation equations were also derived for this analysis. However, the first order perturbations in this analysis were excited by discharge-pressure perturbations instead of impeller precession. The impeller discharge excitation was defined as a precessing harmonic pressure oscillation with n nodes and a precessional frequency of Ω.

Results from the analysis due to perturbed flow in the leakage path caused by oscillations in the impeller discharge pressure show that the peak pressure oscillation occur near the exit ring seal. The pressure oscillations from the impeller were shown to depend on the circumferential velocity of the fluid entering the seal, the Fourier coefficient, n, and the relative closeness to the first resonant frequency of the fluid to the peak precessional frequency of the rotating pressure field. Note that n represents both the Fourier coefficient used by Childs and Bolleter's $n = |n_1 - n_2|$.

Acoustic modes are produced by the interaction of fluid inertia and compressibility. Thompson (1988) explains that the wave equation, the fundamental equation of acoustics, is obtained by assuming that the convective acceleration terms are negligible compared with the temporal acceleration terms. For ordinary acoustic analysis, Thompson states that this assumption is "highly satisfactory" for fluid flow characterized by a low Mach number, typically $M^2 \ll 0.1$. By removing the convective, Coriolis, and centrifugal acceleration terms from a modified general perturbation (compressible) version of Childs' model, a similar wave equation can be obtained. This resulting equation, in theory, can be used for an "acoustic" analysis of the flow fields.

San Andres (1991) developed a solution procedure for a model of fluid flow in turbulent hydrostatic bearings and annular seals operating with cryogenic barotropic fluids. He used a 32-term equations-of-state program provided by NBS Standard Reference Data Base for prediction of the properties of LH_2, LO_2, LN_2, and other fluids at different pressures and temperatures. The code, MIPROPS, delivers fluid properties which are used in the analysis procedure. In addition to obtaining the fluid properties from MIPROPS for use in a compressible model, San Andres also considered the properties of the working fluid as a linear function of pressure. From his results, San Andres found that for highly compressible fluids, such as liquid hydrogen, the barotropic properties model based on an equation of state gave accurate leakage and force response for bearings and seals with a large pressure differential.

CHAPTER III
OBJECTIVES

This research will introduce compressibility of the working fluid in the leakage path as an extension to the analyses performed by Childs (1989, 1992). The results will provide information concerning the relationship between an incompressible, a compressible, and an acoustic model with liquid hydrogen as the working fluid. The results will also provide information regarding the cause of the unusual behavior exhibited by the KEL-F plastic rotor element and verify the validity of Thompson's assessment concerning the effects of fluid mechanics and acoustics. This research project will also analyze the effects of the centrifugal acceleration modes and acoustic modes of a barotropic fluid in the leakage path between a shrouded pump impeller and its housing.

The results obtained from a compressible-flow model will be compared with the results of an incompressible model. The compressible-flow model will also be reduced to an acoustics model, the results of which will be compared to the compressible-flow model. This comparison will be performed for two different perturbation excitations: (a) a precessional excitation involving an orbital motion of the rotor, and (b) a pressure oscillation excitation, involving perturbation of the discharge or inlet pressure of the leakage path. The geometric and operating characteristics of the first stage impeller of the SSME HPFTP will provide the parameters used for the governing equations.

A bulk-flow model will be developed and used to simulate the leakage path inside the first impeller stage of the Space Shuttle Main Engine Turbopump. Results from the computation should indicate if any interaction exists between acoustic and centrifugal acceleration modes, and the influence of fluid mechanics terms (convective, Coriolis, or centrifugal acceleration terms) on acoustic modes.

CHAPTER IV

GEOMETRIC AND OPERATING CHARACTERISTICS

Figure 4 shows the first-stage impeller of the Space Shuttle Main Engine Turbopump. The impeller measures 0.3048 m in diameter at the exit (leakage path inlet) and 0.1905 m in diameter at the seal inlet (leakage path exit). The impeller is also characterized by 24 impeller blades and 13 diffuser vanes. At full power levels, this stage operates at 34,000 rpm, with an inlet pressure at the entrance to the leakage path of 13.79 MPa and a discharge pressure of 1.72 MPa at the exit of the wearing ring seal. Operating at a pump speed of 34,000 rpm, the resultant velocity vector of the liquid hydrogen inside the leakage path is calculated to be about 0.4 times the acoustic velocity of liquid hydrogen.

The wearing ring seal contains four steps, measuring 0.1915, 0.185, 0.1786, and 0.172 m in diameter, which accommodate four teeth at the end of the impeller blade. The radial clearances between the seal and the rotor teeth are estimated to be 0.229 mm (0.009 in), accounting for radial expansion of the rotor during operation.
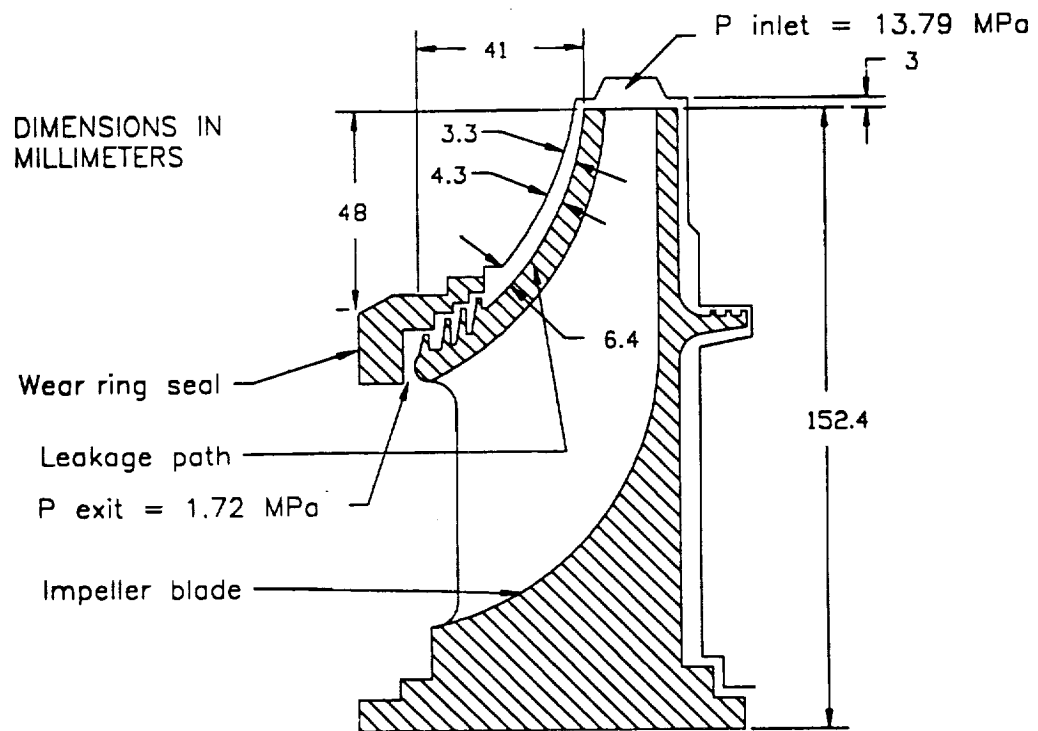
Figure 4 - SSME HPFTP first impeller stage

CHAPTER V

BULK FLOW MATHEMATICAL MODEL

Childs' governing equations will be modified for this project to reflect a bulk flow model operating with a barotropic fluid. As in Childs' analysis, these equations will be nondimensionalized and perturbed to yield zeroth and first-order governing equations.

5.1 General Governing Equations

Using the approach taken by Childs (1989), the governing equations are:

- *Continuity Equation*

$$\frac{\partial \rho H}{\partial t} + \frac{\partial}{\partial S}(\rho U_s H) + \frac{1}{R}\frac{\partial}{\partial \Theta}(\rho U_\theta H) + \frac{H}{R}\frac{\partial R}{\partial S}\rho U_s = 0 \tag{1}$$

- *Path-Momentum Equation*

$$-H\frac{\partial P}{\partial S} = -\rho H\frac{U_\theta^2}{R}\frac{dR}{dS} + \tau_{ss} + \tau_{sr} + \rho H\left(\frac{\partial U_s}{\partial t} + \frac{\partial U_s}{\partial \Theta}\frac{U_\theta}{R} + \frac{\partial U_s}{\partial S}U_s\right) \tag{2}$$

- *Circumferential-Momentum Equation*

$$-\frac{H}{R}\frac{\partial P}{\partial \Theta} = \tau_{\theta s} + \tau_{\theta r} + \rho H\left(\frac{\partial U_\theta}{\partial t} + \frac{\partial U_\theta}{\partial \Theta}\frac{U_\theta}{R} + \frac{\partial U_\theta}{\partial S}U_s + \frac{U_\theta U_s}{R}\frac{\partial R}{\partial S}\right) \tag{3}$$

An additional governing equation is obtained by using MIPROPS to obtain the properties of liquid hydrogen.

• *Equations of State*

$$\rho = \rho\left(P, \overline{T}^\circ\right)$$

$$\mu = \mu\left(P, \overline{T}^\circ\right) \tag{4}$$

With the exception of the addition of ρ to the continuity equation, Eqs. (1-3) are identical to Childs' (1989). The path and circumferential-momentum equations do not change from Childs' model because the density (ρ) drops out of the momentum equations when the continuity equation is used to simplify them.

The equations of state in Eq. (4) define the density and viscosity for the bulk-flow model. The variation in density of the fluid in the model will be implemented by assuming that the working fluid is barotropic. Here, the variation in density of the working fluid will be modelled as a function of pressure and a constant temperature only. In this investigation, the MIPROPS code calculates the value of density and viscosity at a constant temperature of 23.37 K with varying input pressures, and returns values of density and viscosity to the main program. The variation of viscosity with respect to pressure were very slight; therefore, viscosity was kept constant.

$H(S, \theta, t)$ in the governing equations defines the clearance between the impeller and the housing. Nondimensionalization of this variable is given in the nomenclature and also later in this text.

Hir's (1973) definitions were used to define the shear stress components of the rotor and stator surfaces. The equations shown below define the shear stress acting on the impeller and its housing. The first subscript in the equations denotes the direction of fluid flow (path and circumferential), and the second subscript refers to the surface (stator and rotor), respectively.

$$\tau_{ss} = \frac{ns}{2} \rho \, U_s^2 R_a^{ns} \left[1 + \left(U_\theta / U_s\right)^2\right]^{\frac{ms+1}{2}} \tag{5}$$

$$\tau_{sr} = \frac{nr}{2}\rho U_s^2 R_\alpha^{mr}\left\{1 + [(U_\theta - R\omega)/U_s]^2\right\}^{\frac{mr+1}{2}} \tag{6}$$

$$\tau_{\theta s} = \frac{ns}{2}\rho U_\theta U_s R_\alpha^{ms}\left[1 + (U_\theta/U_s)^2\right]^{\frac{ms+1}{2}} \tag{7}$$

$$\tau_{\theta r} = \frac{nr}{2}\rho U_s(U_\theta - R\omega)R_\alpha^{mr}\left\{1 + [(U_\theta - R\omega)/U_s]^2\right\}^{\frac{mr+1}{2}} \tag{8}$$

Reynolds' number used in these equations is represented by,

$$R_\alpha = 2HU_s/\nu \tag{9}$$

Boundary Conditions

The pressure drop of the inlet to the leakage path provides the inlet boundary condition (s=0) given by the relationship,

$$P_s - P_0(0,\theta,t) = \rho(1 + \xi)U_{s0}^2(0,\theta,t)/2 \tag{10}$$

The exit wearing-ring seal defines the following exit boundary condition,

$$P(L_s,\theta,t) - P_e = \frac{\rho}{2}C_{de}U_s^2(L_s,\theta,t) \tag{11}$$

These boundary conditions apply directly for precession excitations.

For the analysis which examines the changes in (u_s, u_θ, p) due to changes in the impeller's discharge P_e or inlet pressure P_s, the following boundary conditions are

stated for the inlet and exit, respectively,

$$P_s(\theta,t) - P_0(0,\theta,t) = \rho(1+\xi)U_{s0}^2(0,\theta,t)/2 \tag{12}$$

$$P(L_s,\theta,t) - P_e(\theta,t) = \frac{\rho}{2}C_{de}U_s^2(L_s,\theta,t) \tag{13}$$

Eqs. (12-13) differ from Eqs. (10-11) because P_e and P_s are now also functions of time.

5.2 General Perturbed Equations - Nondimensionalization and Perturbation Analysis

Introducing the following variables into Eqs. (1-8),

$$\begin{aligned}
&u_s = U_s/V_i, \quad u_\theta = U_\theta/R_i\omega, \quad p = P/\rho V_i^2, \quad \bar{\rho} = \rho/\rho_i \\
&h = H/C_i, \quad s = S/L_s, \quad r = R/R_i \quad (14) \\
&\tau = \omega t, \quad b = V_i/R_i\omega, \quad T = L_s/V_i
\end{aligned}$$

yields nondimensional governing equations.

The perturbation variables used to obtain zeroth and first-order equations are defined by,

$$\begin{aligned}
&u_s = u_{s0} + \epsilon u_{s1}, \quad h = h_0 + \epsilon h_1, \quad \bar{\rho} = \bar{\rho}_0 + \epsilon\bar{\rho}_1 \\
&u_\theta = u_{\theta 0} + \epsilon u_{\theta 1}, \quad p = p_0 + \epsilon p_1
\end{aligned} \tag{15}$$

where ϵ is the perturbation coefficient to be defined separately below for precession and discharge-pressure excitation.

5.2.1 Zeroth Order Solution

The zeroth-order equations are the same for the precession and exit-pressure excitations.

5.2.1.1 Zeroth-Order Equations

The path and circumferential velocity distribution and the leakage rate for a centered impeller position are defined by the following zeroth-order governing equations.

- *Continuity Equation*

$$rh_0 u_{s0} \bar{\rho}_0 = 1 \qquad (16)$$

- *Path-Momentum Equation*

$$-\frac{1}{\bar{\rho}_0}\frac{dp_0}{ds} = u_{s0}\frac{du_{s0}}{ds} - \frac{1}{r}\frac{dr}{ds}\left(\frac{u_{\theta 0}}{b}\right)^2 + \frac{(\sigma_s + \sigma_r)}{2}u_{s0}^2 \qquad (17)$$

- *Circumferential-Momentum Equation*

$$2\frac{du_{\theta 0}}{ds} + 2\frac{u_{\theta 0}}{r}\frac{dr}{ds} + \left[\sigma_r(u_{\theta 0} - r) + \sigma_s u_{\theta 0}\right] = 0 \qquad (18)$$

where

$$\sigma_s = (L_s/H_0)\lambda_s, \quad \sigma_r = (L_s/H_0)\lambda_r$$

$$\lambda_s = nsR_{a0}^{ms}\left[1 + (u_{\theta 0}/bu_{s0})^2\right]^{\frac{ms+1}{2}} \qquad (19)$$

$$\lambda_r = nsR_{a0}^{mr}\left\{1 + \left[(u_{\theta_0} - r)/bu_{s0}\right]^2\right\}^{\frac{mr+1}{2}}$$

- *Equation of State*

$$\bar{\rho} = \bar{\rho}(p, \bar{T}^\circ) \qquad (20)$$

Eq. (19) represents friction factor definitions for the stator and rotor surfaces, respectively, introduced in Eqs. (5-8).

5.2.1.2 Zeroth-Order Solution

The zeroth-order continuity Eq. (16) can also be expressed as,

$$\frac{du_{s0}}{ds} = -u_{s0}\left[\frac{1}{h_0}\frac{dh_0}{ds} + \frac{1}{\bar{\rho}_0}\frac{d\bar{\rho}_0}{ds} + \frac{1}{r}\frac{dr}{ds}\right] \tag{21}$$

This equation can be substituted into Eq. (17) to obtain

$$-\frac{1}{\bar{\rho}_0}\frac{dp_0}{ds} = -u_{s0}^2\left[\frac{1}{h_0}\frac{dh_0}{ds} + \frac{1}{\bar{\rho}_0}\frac{d\bar{\rho}_0}{ds} + \frac{1}{r}\frac{dr}{ds}\right] - \frac{1}{r}\frac{dr}{ds}\left(\frac{u_{\theta0}}{b}\right)^2 + \frac{(\sigma_s + \sigma_r)}{2}u_{s0}^2 \tag{22}$$

The governing zeroth-order equations now reduce to two governing equations, consisting of Eq. (18) and Eq. (22). Eq. (20) defines ρ solely as a function of p and provides the density used in Eq. (18) and Eq. (22).

Boundary Conditions

The inlet boundary condition for the zeroth-order pressure relationship can be expressed from Eq. (10) as,

$$p_0(0) = \frac{P_s}{\rho_i V_i^2} - (1 + \xi)\frac{u_{s0}^2(0)}{2} \tag{23}$$

The zeroth-order solutions are obtained by solving Equations (18) and (22) iteratively. An initial (s=0) fluid velocity V_i is estimated which then defines $u_{s0}(s)$. A specified $u_{\theta0}(0)$ and the calculated p_0 from Eq. (23) are used to numerically integrate the zeroth-order equations (18) and (22) from the path entrance (s=0), to the path exit (s=1). The procedure is continued with revised values of V_i until convergence is obtained between the prescribed and the calculated exit pressure.

5.2.1.3 Zeroth-Order Results

The zeroth-order results provide the mass flow rate through the leakage path.

The discharge coefficient C_{dc} used in this analysis was obtained by using the leakage rate through the wearing ring seal. The leakage through the wearing ring seal of the SSME HPFTP was calculated using a seal leakage code developed by Morrison et al. (1983), and this value was used to calculate the discharge coefficient at specific impeller operating conditions. The seal leakage code uses the geometry of the seal and the operating conditions, i.e., inlet and exit pressures, viscosity, density, etc. to calculate the leakage rate through the seal. Note that this seal leakage code treats the working fluid as incompressible.

The seal leakage code yielded several mass flow rates for the prescribed geometry and operating conditions, depending upon the pressure drop across the impeller and the wearing ring seal. Several discharge coefficients were tested in the model to match the flow rate through the impeller leakage path and the flow rate through the seal. Once the two flow rates converged, the resulting C_{dc} was used in the model as an exit restriction boundary condition. The mass flow rate through the seal was found to be 1.6373 kg/s, with the resulting C_{dc} being 7039.6, and inlet and exit pressure of the seal being 8.101 MPa and 1.72 MPa, respectively. This pressure drop across the seal represents about one third of the total pressure drop across the entire impeller leakage path.

Zeroth-order pressure solutions for the incompressible and compressible models are shown in Figure 5. The nondimensional path velocity along the leakage path is given in Figure 6, and the zeroth-order circumferential path velocity is shown in Figure 7. For the incompressible model, a mean value for the density of liquid hydrogen inside the impeller leakage path was used to obtain the results shown.

The results of the compressible model vary only slightly from the incompressible model for the zeroth-order solution. The pressure distribution across the leakage path shows the same trend and approximately the same magnitude of pressure drop, but not exactly the same inlet and exit pressure values. The C_{dc} found earlier provides the exit restriction for the seal and therefore is used for both models. Because the incompressible model uses an average density along the leakage path, the inlet and exit densities for the two models will be slightly different. This accounts for
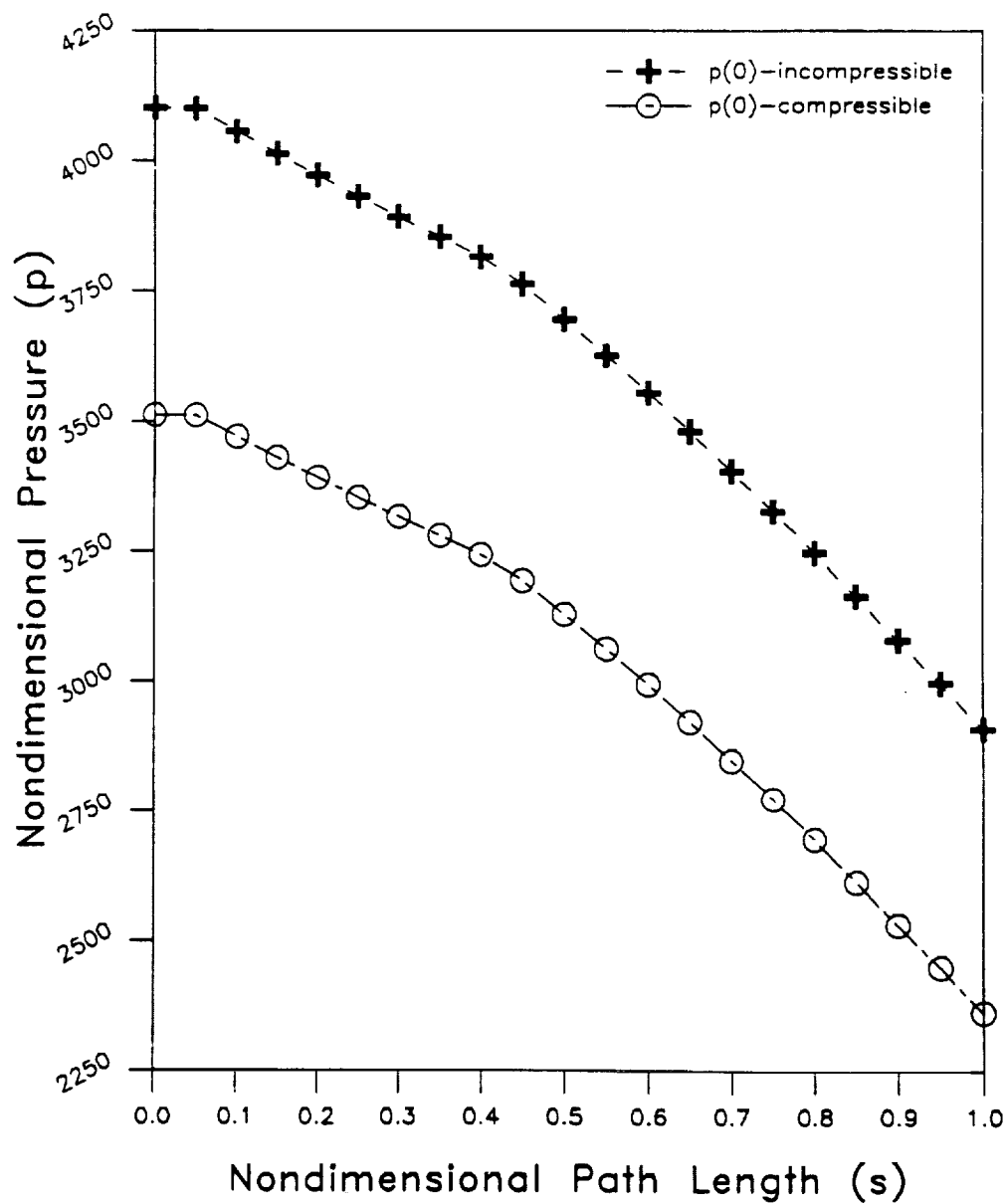
Figure 5 - Zeroth-order pressure p distribution along leakage path for compressible and incompressible models for $u_{to}(0) = 0.7$
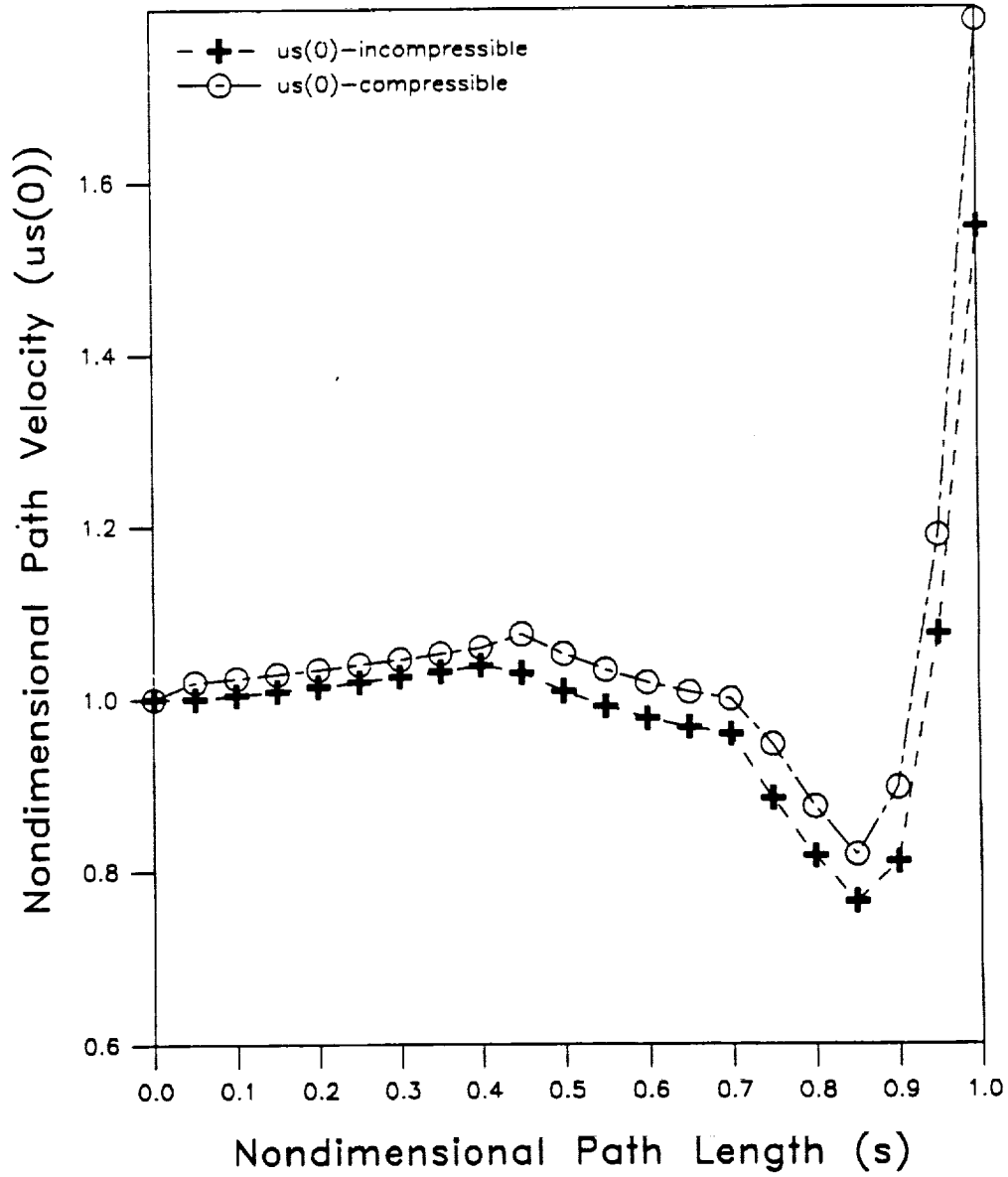
Figure 6 - Zeroth-order path velocity (u_{s0}) distribution along leakage path for compressible and incompressible models for $u_{\theta 0}(0) = 0.7$
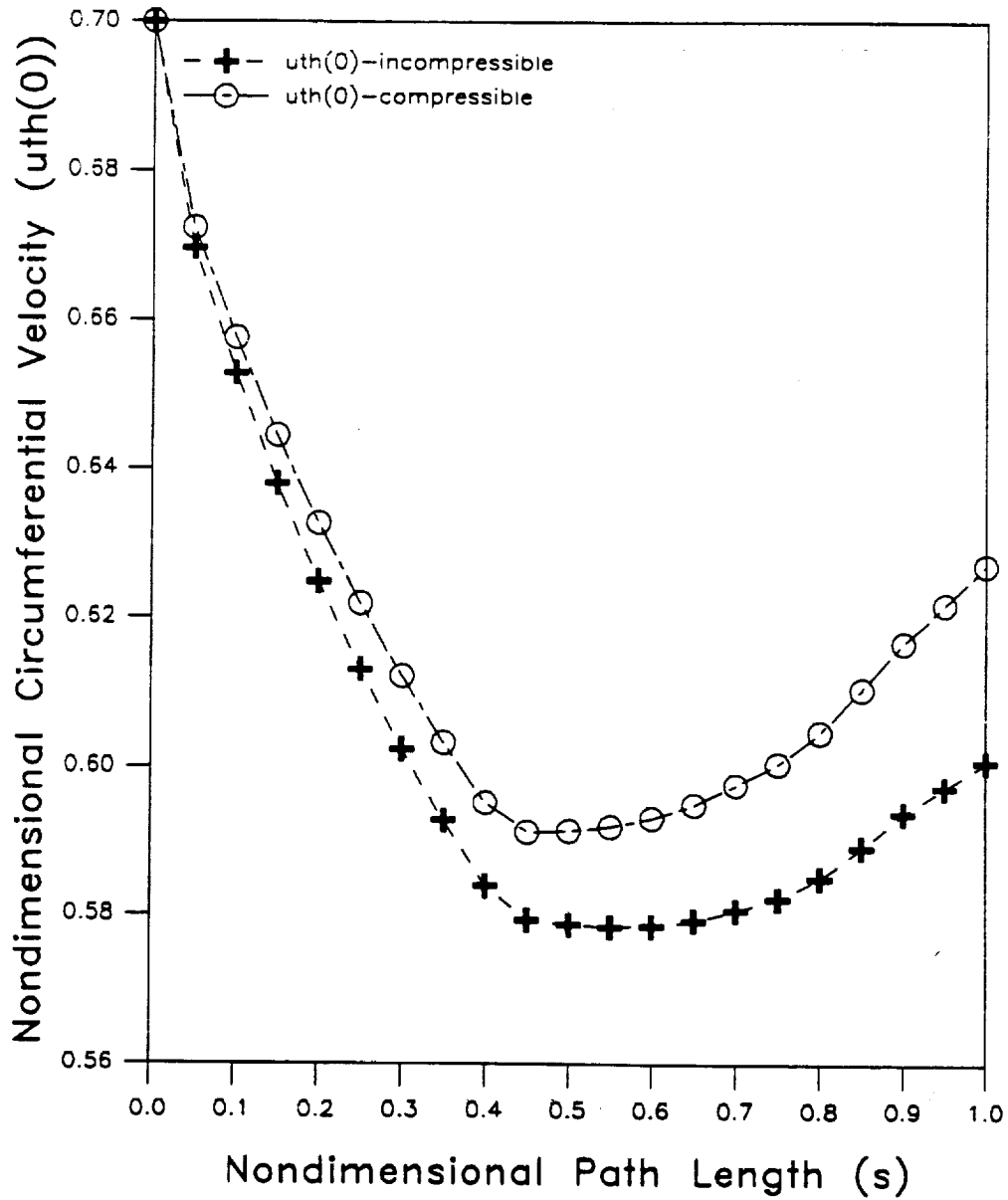
Figure 7 - Zeroth-order circumferential velocity distribution along leakage path for compressible and incompressible models for $u_{\theta o}(0) = 0.7$

the difference in the dimensionless pressure magnitudes shown in Figure 5. The dimensional pressures at the inlet are almost exactly the same value, confirming the inlet boundary condition. As shown in Figure 6 and Figure 7, the zeroth-order path velocity and the zeroth-order circumferential velocity are not affected significantly by compressibility.

5.2.2 First-Order Equations

First-order governing equations define the path and circumferential velocity and pressure distribution along the leakage path due to perturbed clearance function or perturbed discharge-pressure.

First-order perturbation equations obtained by the perturbation expansion of Eq. (14) are

- *Continuity Equation*

$$
\bar{\rho}_0 \frac{\partial h_1}{\partial \tau} + h_0 \frac{\partial \bar{\rho}_1}{\partial \tau} + \frac{1}{r}\left[u_{\theta 0} h_0 \frac{\partial \bar{\rho}_1}{\partial \theta} + h_0 \bar{\rho}_0 \frac{\partial u_{\theta 1}}{\partial \theta} + u_{\theta 0} \bar{\rho}_0 \frac{\partial h_1}{\partial \theta} \right]
$$
$$
+ \frac{1}{T\omega}\left[\frac{\partial(\bar{\rho}_0 u_{s0} h_1)}{\partial s} + \frac{\partial(\bar{\rho}_0 u_{s1} h_0)}{\partial s} + \frac{\partial(\bar{\rho}_1 u_{s0} h_0)}{\partial s} \right] + \frac{1}{T\omega} \frac{dr}{r ds}(u_{s0}\bar{\rho}_0 h_1 + u_{s1}\bar{\rho}_0 h_0 + u_{s0}\bar{\rho}_1 h_0) = 0
$$

(24)

- *Path-Momentum Equation*

$$
\frac{1}{\partial \bar{\rho}_0} \frac{\partial p_1}{\partial s} + u_{\theta 1} A_{2s} + u_{s1} A_{3s} + \bar{\rho}_1 A_{4s} + \left[T\omega \frac{\partial u_{s1}}{\partial \tau} + T\omega \frac{u_{\theta 0}\partial u_{s1}}{r\partial \theta} + u_{s0}\frac{\partial u_{s1}}{\partial s} \right] = h_r A_{1s}
$$

(25)

- *Circumferential-Momentum Equation*

$$
\frac{b}{r}\frac{L_s}{R_i} \frac{\partial p_1}{\bar{\rho}_0 \partial \theta} + u_{\theta 1} A_{2\theta} + u_{s1} A_{3\theta} + \bar{\rho}_1 A_{4\theta} + \left[T\omega \frac{\partial u_{\theta 1}}{\partial \tau} + T\omega \frac{u_{\theta 0}}{r} \frac{\partial u_{\theta 1}}{\partial \theta} + u_{s0}\frac{\partial u_{\theta 1}}{\partial s} \right] = h_r A_{1\theta}
$$

(26)

- *Equation of State*

$$\frac{\partial \tilde{\rho}_1}{\partial s} = \frac{d\tilde{\rho}_1}{dp}\frac{\partial p_1}{\partial s}, \qquad \frac{\partial \tilde{\rho}_1}{\partial \tau} = \frac{d\tilde{\rho}_1}{dp}\frac{\partial p_1}{\partial \tau}, \qquad \frac{\partial \tilde{\rho}_1}{\partial \theta} = \frac{d\tilde{\rho}_1}{dp}\frac{\partial p_1}{\partial \theta} \tag{27}$$

With the exceptions of A_{4s} and $A_{4\theta}$, which are defined in the appendix, the parameters A_{1s}, A_{2s}, etc., in these equations can be found in Childs (1989).

The dependency of $\tilde{\rho}$ with respect to s, τ, and θ in Eq. (24-26) are eliminated from the governing equations by applying the definitions of Eq. (27). The relationship between $\tilde{\rho}$ and p in Eq. (27) was obtained from the results produced by MIPROPS.

CHAPTER VI

FIRST ORDER EQUATIONS AND SOLUTIONS FOR GENERAL PERTURBED COMPRESSIBLE MODELS

This chapter provides the first order equations and solutions for precession excitation and pressure excitation cases for the general perturbation (compressible) models. Results for both excitation cases are presented using an inlet tangential velocity of $u_{\theta 0}(0) = 0.7$. The radial and circumferential-force coefficient response curves represent the nondimensional reaction force acting on the impeller face in the respective directions versus nondimensional frequency ratio, f.

For the first-order solution analysis, a separation of variable approach was used to obtain complex ordinary differential equations. The resulting coupled equations were integrated to obtain the nondimensional radial and circumferential force response coefficients. The calculated results from the first-order precession excitation and the pressure excitation of the general perturbed bulk flow model provide predictions which can be used to qualify and quantify the effects of fluid compressibility in the model.

6.1 Precession Excitation: General-Perturbation Model

The precession excitation of the general perturbed model uses the perturbed clearance function,

$$\epsilon h_1 = h_{1c}(s,\tau)\cos\theta + h_{1s}(s,\tau)\sin\theta \tag{28}$$

as the excitation.

The theta dependency of Eqs. (24-26) can be eliminated by substituting the following solution format

$$
\begin{aligned}
u_{s1} &= u_{s1c}\cos\theta + u_{s1s}\sin\theta & u_{\theta 1} &= u_{\theta 1c}\cos\theta + u_{\theta 1s}\sin\theta \\
p_1 &= p_{1c}\cos\theta + p_{1s}\sin\theta & \bar{\rho}_1 &= \bar{\rho}_{1c}\cos\theta + \bar{\rho}_{1s}\sin\theta
\end{aligned}
\tag{29}
$$

into Eqs. (24-26), which yields six real equations.

Three complex equations in the independent variables s and τ can be obtained by introducing the complex variables

$$\underline{u}_{s1} = u_{s1c} + j u_{s1s}, \quad \underline{u}_{\theta 1} = u_{\theta 1c} + j u_{\theta 1s}, \quad \tilde{\underline{\rho}}_1 = \tilde{\rho}_{1c} + j \tilde{\rho}_{1s}$$

$$\underline{P}_1 = P_{1c} + j P_{1s}, \quad \underline{h}_1 = h_{1c} + j h_{1s}$$

(30)

These complex equations in the independent variables s and τ are

$$\frac{\partial \underline{u}_{s1}}{\partial s} - \frac{j\omega T}{r}\underline{u}_{\theta 1} + \underline{u}_{s1}\left[\frac{1}{h_0}\frac{\partial h_0}{\partial s} + \frac{1}{\tilde{\rho}_0}\frac{\partial \tilde{\rho}_0}{\partial s} + \frac{1}{r}\frac{\partial r}{\partial s}\right] - \tilde{\underline{\rho}}_1\left[\frac{u_{s0}}{\tilde{\rho}_0^2}\frac{\partial \tilde{\rho}_0}{\partial s} + j\frac{\omega T}{\tilde{\rho}_0 r}u_{\theta 0}\right]$$

$$+ \frac{\omega T}{\tilde{\rho}_0}\frac{d\tilde{\rho}_1}{dP_1}\frac{\partial \underline{P}_1}{\partial \tau} + \frac{u_{s0}}{\tilde{\rho}_0}\frac{\partial \tilde{\underline{\rho}}_1}{\partial s} = \underline{h}_1\left[\frac{u_{s0}}{h_0^2}\frac{\partial h_0}{\partial s} + j\frac{\omega T}{h_0 r}u_{\theta 0}\right] - \frac{\omega T}{h_0}\frac{\partial \underline{h}_1}{\partial \tau} - \frac{u_{s0}}{h_0}\frac{\partial \underline{h}_1}{\partial s}$$

(31)

$$\frac{1}{\tilde{\rho}_0}\frac{\partial \underline{P}_1}{\partial s} + \underline{u}_{\theta 1}A_{2s} + \underline{u}_{s1}A_{3s} + \tilde{\underline{\rho}}_1 A_{4s} + \left[T\omega\frac{\partial \underline{u}_{s1}}{\partial \tau} - jT\omega\frac{u_{\theta 0}}{r}\underline{u}_{s1} + u_{s0}\frac{\partial \underline{u}_{s1}}{\partial s}\right] = \underline{h}_1 A_{1s}$$

(32)

$$-\frac{b}{r}\frac{L_s}{R_i}\frac{\underline{P}_1}{\tilde{\rho}_0} + \underline{u}_{\theta 1}A_{2\theta} + \underline{u}_{s1}A_{3\theta} + \tilde{\underline{\rho}}_1 A_{4\theta} + \left[T\omega\frac{\partial \underline{u}_{\theta 1}}{\partial \tau} - jT\omega\frac{u_{\theta 0}}{r}\underline{u}_{\theta 1} + u_{s0}\frac{\partial \underline{u}_{\theta 1}}{\partial s}\right] = \underline{h}_1 A_{1\theta}$$

(33)

Since the equation of state is a function of pressure and a constant temperature only, it can be modified as shown in Eq. (27) and used to remove the dependency of $\tilde{\rho}_1$ from s in Eq. (31). Further simplification of Eqs. (33-35) can be made by using the following definitions provided by Childs (1989)

$$\epsilon \underline{h}_1 = -q\left(\frac{L}{L_s}\right)\frac{dz}{ds}$$

(34)

$$\epsilon\frac{\partial \underline{h}_1}{\partial s} = -q\left(\frac{L}{L_s}\right)\frac{d^2 z}{ds^2}$$

(35)

where

$$q = x + jy \tag{36}$$

Eq. (36) represents the physical motion of the rotor in the x and y directions, shown in Figure 1.

Assuming a harmonic seal motion of the form

$$q = q_0 e^{jft}, \quad f = \Omega/\omega \tag{37}$$

the corresponding harmonic solutions can be stated,

$$u_{s1} = \bar{u}_{s1} e^{jft}, \quad u_{\theta1} = \bar{u}_{\theta1} e^{jft}, \quad p_1 = \bar{p}_1 e^{jft} \tag{38}$$

which yields the following three complex ordinary differential equations of motion,

$$\frac{d}{ds} \left\{ \begin{matrix} \bar{u}_{s1} \\ \bar{u}_{\theta1} \\ \bar{p}_1 \end{matrix} \right\} + [A] \left\{ \begin{matrix} \bar{u}_{s1} \\ \bar{u}_{\theta1} \\ \bar{p}_1 \end{matrix} \right\} = \left(\frac{q_0}{\epsilon} \right) \left\{ \begin{matrix} g_1 \\ g_2 \\ g_3 \end{matrix} \right\} \tag{39}$$

where

$$[A] = \begin{bmatrix} A_{11} & -\dfrac{j\omega T}{r} - A_{12} & -\dfrac{d\tilde{\rho}_0}{ds}\left(\dfrac{u_{s0}}{\tilde{\rho}_0^2}\dfrac{d\tilde{\rho}_0}{ds} + \dfrac{j\omega T u_{\theta0}}{\tilde{\rho}_0 r} \right) + j\omega T\dfrac{d\tilde{\rho}_0}{ds} + A_{13} \\[2ex] \dfrac{A_{3s}}{u_{s0}} & \dfrac{A_{2\theta}}{u_{s0}} + \dfrac{j\Gamma T}{u_{s0}} & A_{4\theta}\dfrac{d\tilde{\rho}_0}{ds} - j\dfrac{bL_s}{r u_{s0}\tilde{\rho}_0 R_l} \\[2ex] A_{31} & A_{32} & \dfrac{A_{4s}}{\tilde{\rho}_0} - \dfrac{A_{33}}{\tilde{\rho}_0}\dfrac{d\tilde{\rho}_0}{ds} \end{bmatrix} \tag{40}$$

$$
\begin{Bmatrix} g_1 \\ g_2 \\ g_3 \end{Bmatrix} = \left(\frac{L}{L_s}\right) \begin{Bmatrix} \dfrac{u_{s0}}{\bar{\rho}_0}\dfrac{d\bar{\rho}_0}{dp_0}G_q + F_2 + j\dfrac{\Gamma T}{h_0}\dfrac{dz}{ds} \\[2ex] -\dfrac{dz}{ds}\dfrac{A_{18}}{u_{s0}} \\[2ex] G_q \end{Bmatrix}
\tag{41}
$$

Elements used in Eqs. (40-41) can be found in Appendix A.

6.1.1 Boundary Conditions

Nondimensional first-order boundary conditions for the precession excitation can be stated from equations (10) and (11) as

$$
\frac{\bar{p}_1(0)}{\left(1 + \dfrac{(1+\xi)}{2}\dfrac{d\bar{\rho}}{dp}\Big|_0\right)} = -(1+\xi)\bar{u}_{s1}(0)
\tag{42}
$$

$$
\frac{\bar{p}_1(1)}{\left(1 + \dfrac{(1+\xi)}{2}\dfrac{d\bar{\rho}}{dp}\Big|_1\right)} = C_{de}u_{s0}(1)\bar{u}_{s1}(1)
\tag{43}
$$

Additionally, the perturbation entrance circumferential velocity can be stated as zero,

$$
\bar{u}_{\theta 1}(0) = 0
\tag{44}
$$

The solution to this set of equations is obtained by applying the procedure presented by Childs (1989). The solution procedure used to determine the reaction forces and moments are also given by Childs (1989).

6.1.2 First-Order Results

Radial and circumferential force response coefficients for general compressible and incompressible precession excitation models operating with an inlet circumferential velocity of $u_{\theta 0}(0) = 0.7$ are shown in Figure 8 and Figure 9. The results
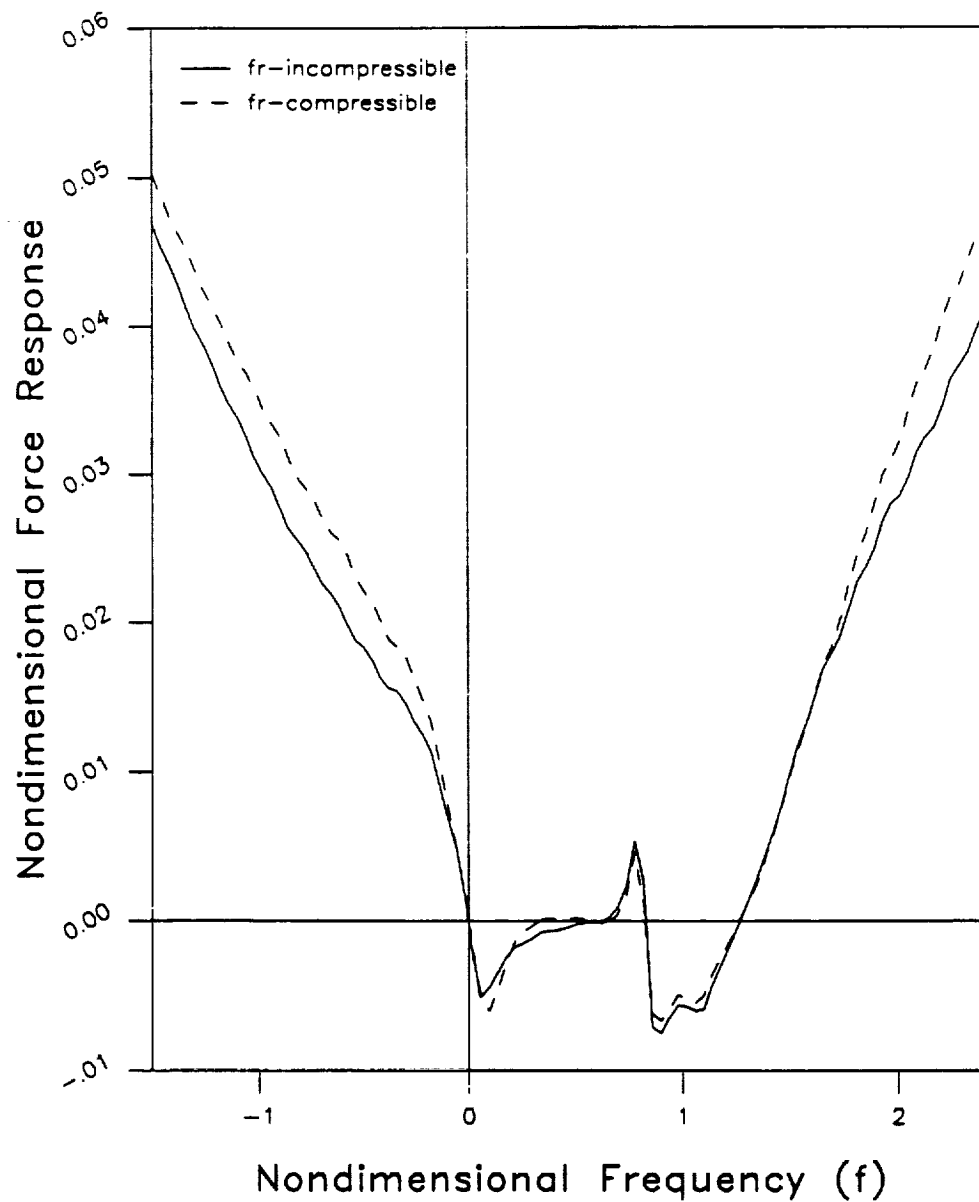
Figure 8 - Radial response for compressible and incompressible models for precession excitation for $u_{\theta o}(0) = 0.7$
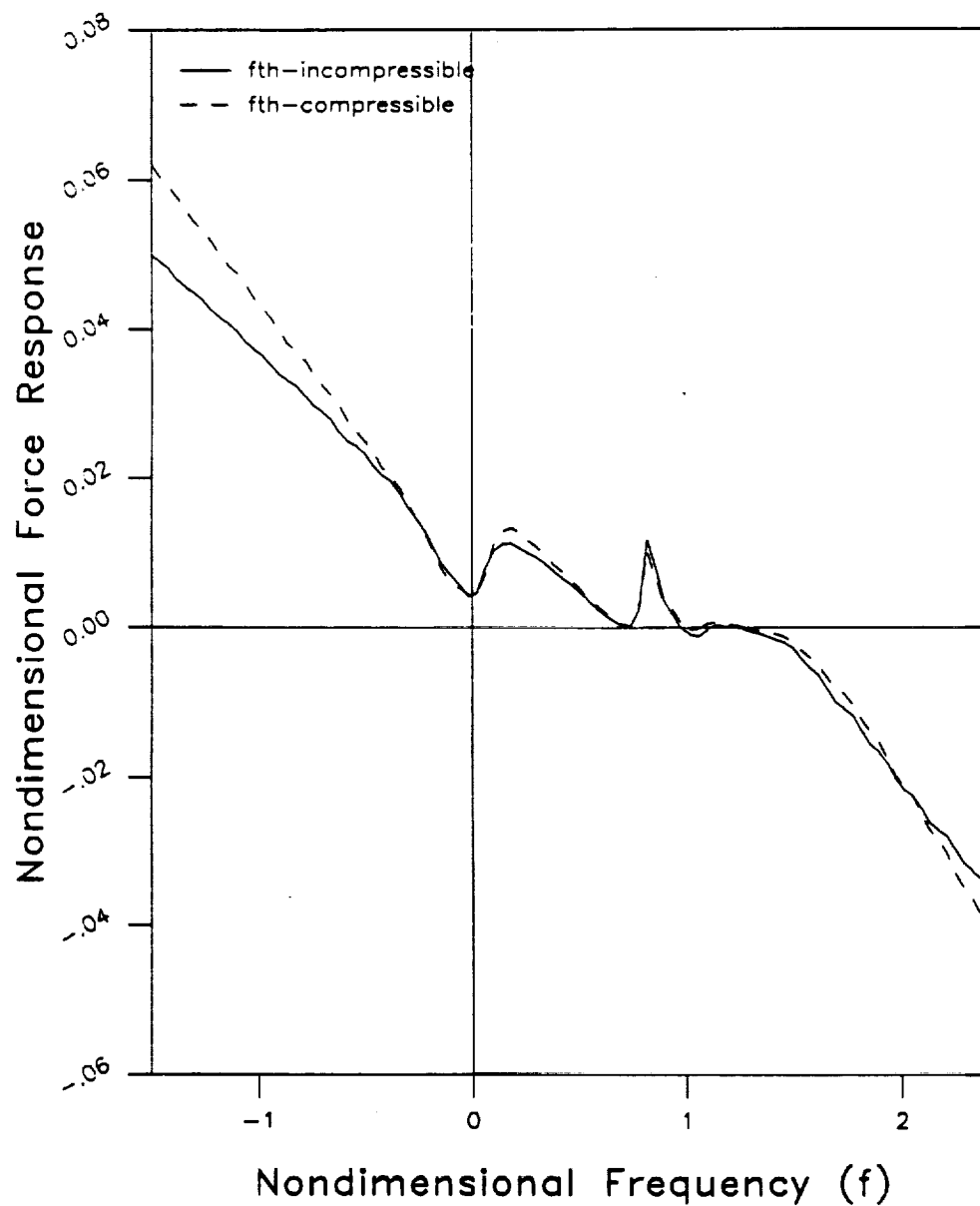
Figure 9 - Circumferential response for compressible and incompressible models for precession excitation for $u_{\theta o}(0) = 0.7$

show that the effects of compressibility do not affect the results of the model to a great extent over the frequency range considered. As with Childs' results, local resonance peaks occur in the response curves. Two local peaks occur in the response curves, at nondimensional frequency ratios of $f = 0.1$ and $f = 0.8$. For low inlet values of circumferential velocity $u_{\theta 0}(0) = 0.5$, the behavior of the response curves of the compressible model is virtually the same as the results shown for an incompressible model shown by Childs (1989), i.e., the resonance in the response curves diminish at lower values of inlet circumferential velocity.

Complex first-order pressure, path velocity, and circumferential velocity for different nondimensional excitation frequencies along the leakage path produced from the first-order perturbation analysis provide approximate complex modes at the resonant frequencies. The real and imaginary parts of these results are used to obtain amplitude and phase plots at the resonant frequencies. Amplitude and phase plots of first-order nondimensional pressure in the leakage path at the frequency ratios of $f = 0.1$ and $f = 0.8$, where the local peaks occur, are shown in Figures 10 and 11. Complex modes for u_{sl} at the same frequency ratios are shown in Figures 12 and 13.

At the frequency ratio of $f = 0.1$, the amplitude of the pressure along the leakage path steadily increases and has a maximum value at the exit of the leakage path. For the frequency ratio of $f = 0.8$, the maximum pressure amplitude occurs near the middle of the leakage path. The mode shape for u_{sl} at $f = 0.1$ shows a slightly decreasing amplitude along the leakage path, with a minor increase in the amplitude at the exit. As with the mode shape for the pressure distribution at $f = 0.8$, the maximum magnitude occurs near the middle of the seal.

As with Childs' model, the resonant peaks found in this analysis can be attributed to the centrifugal acceleration terms. When the centrifugal acceleration terms are removed from the model, the local peaks in the response curves diminish significantly. The mode shapes at $f = 0.8$ do not support the theory that maximum pressure oscillations at the leakage path exit are causing the seal to melt because the maximum amplification occurs near the middle of the leakage path.

Mode Shape

Phase Plot

Figure 10 - Amplitude and phase plot of nondimensional pressure p for precessional excitation of compressible model at $f = 0.1$
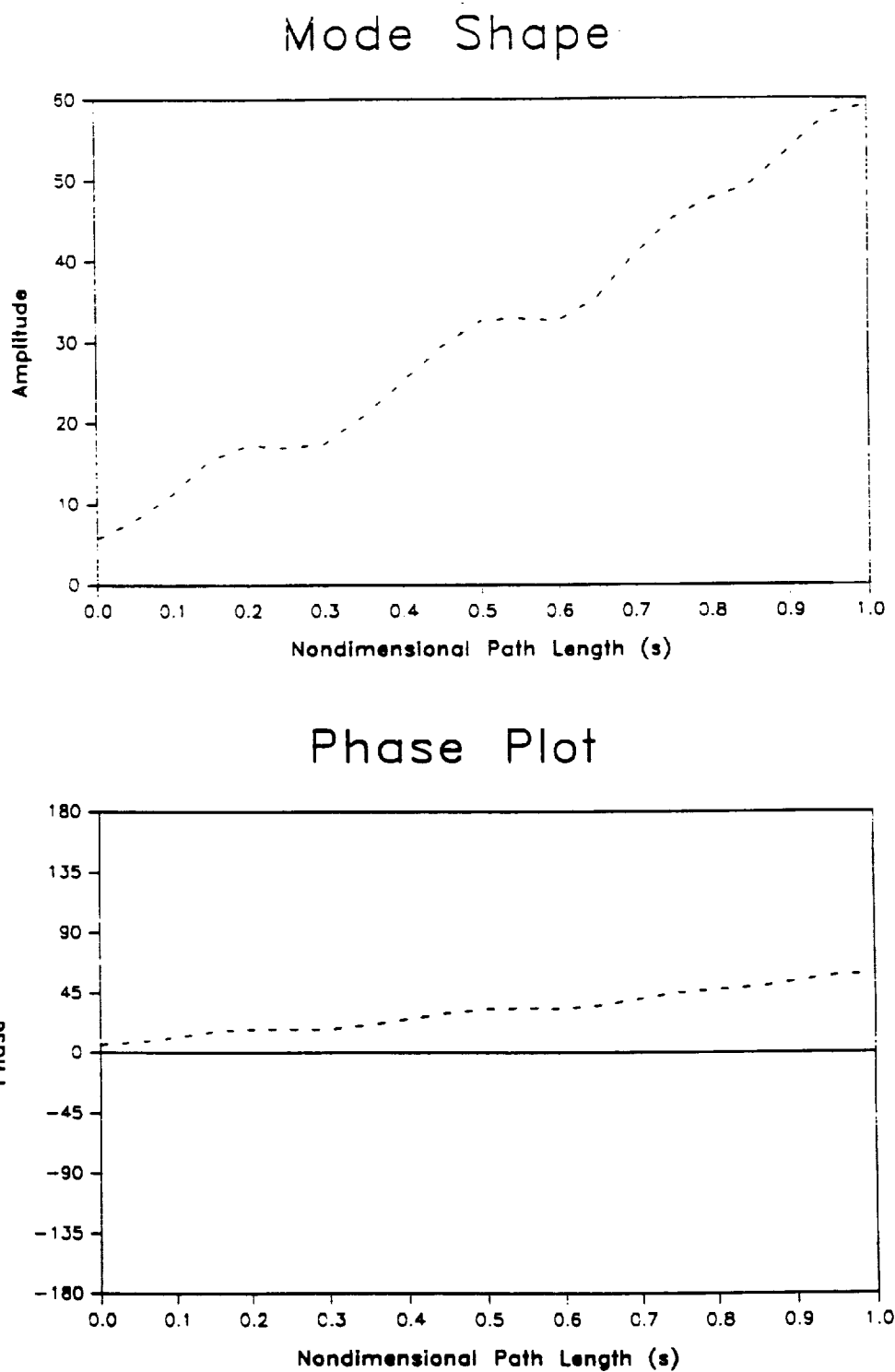
Mode Shape
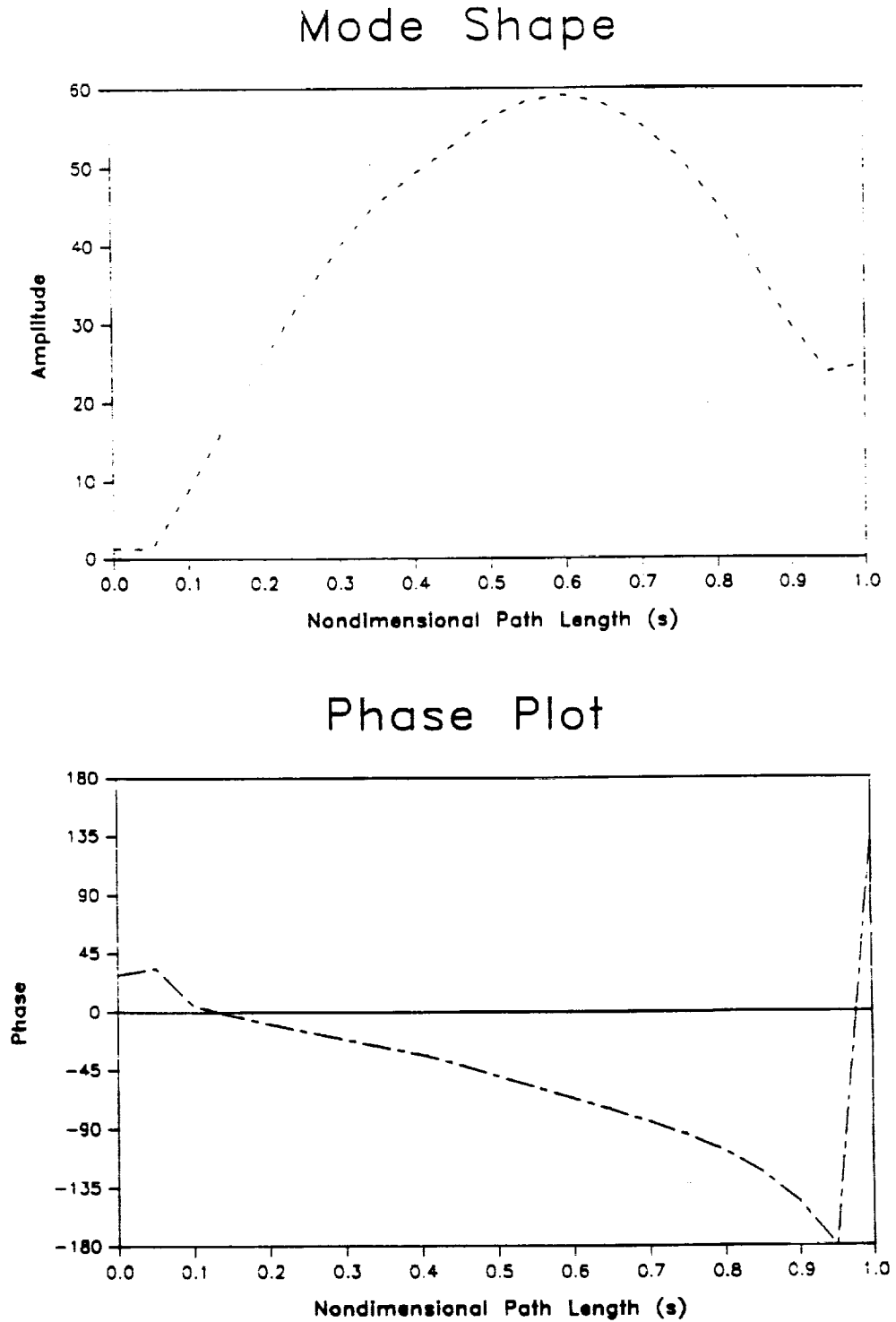
Phase Plot

Figure 11 - Amplitude and phase plot of nondimensional pressure p for precessional excitation of compressible model at $f = 0.8$

Mode Shape

Phase Plot

Figure 12 - Amplitude and phase plot for precessional excitation for path velocity u_{sI} of compressible model at $f = 0.1$

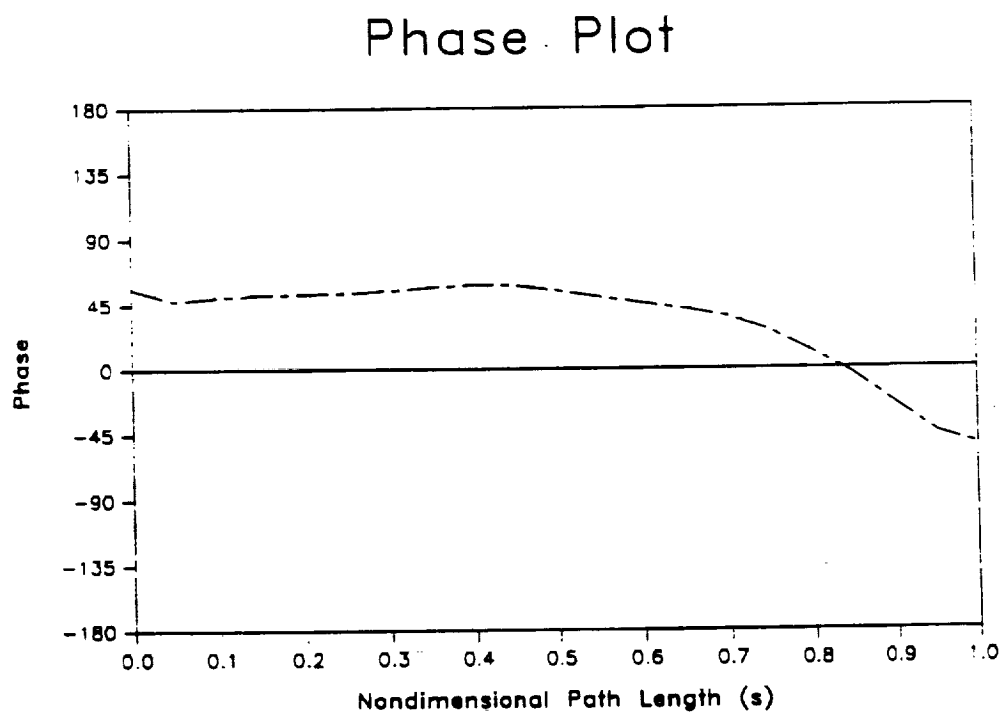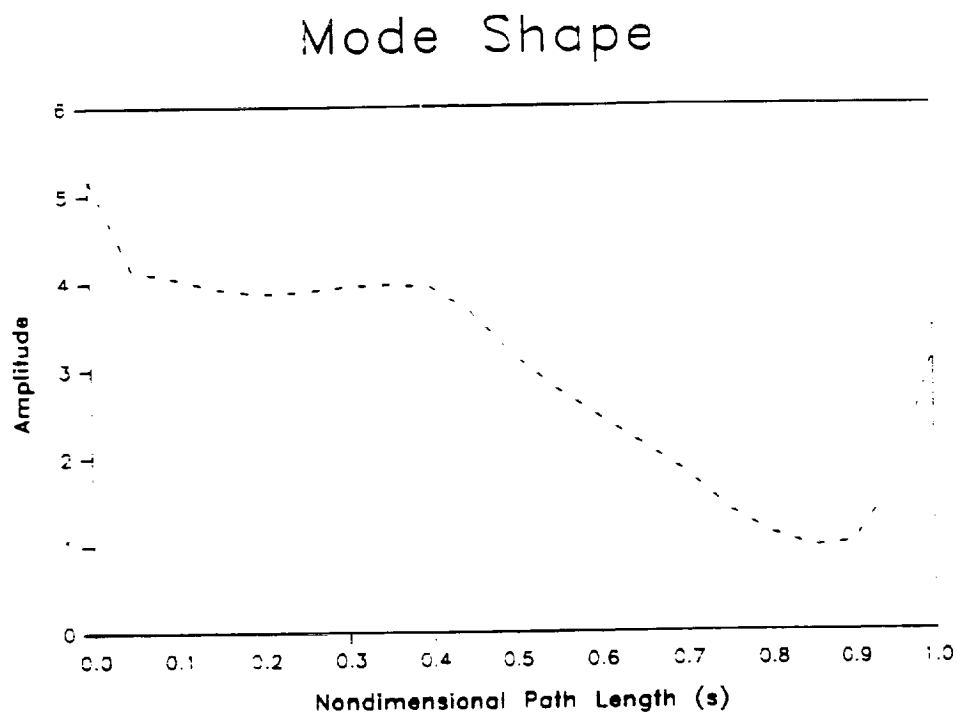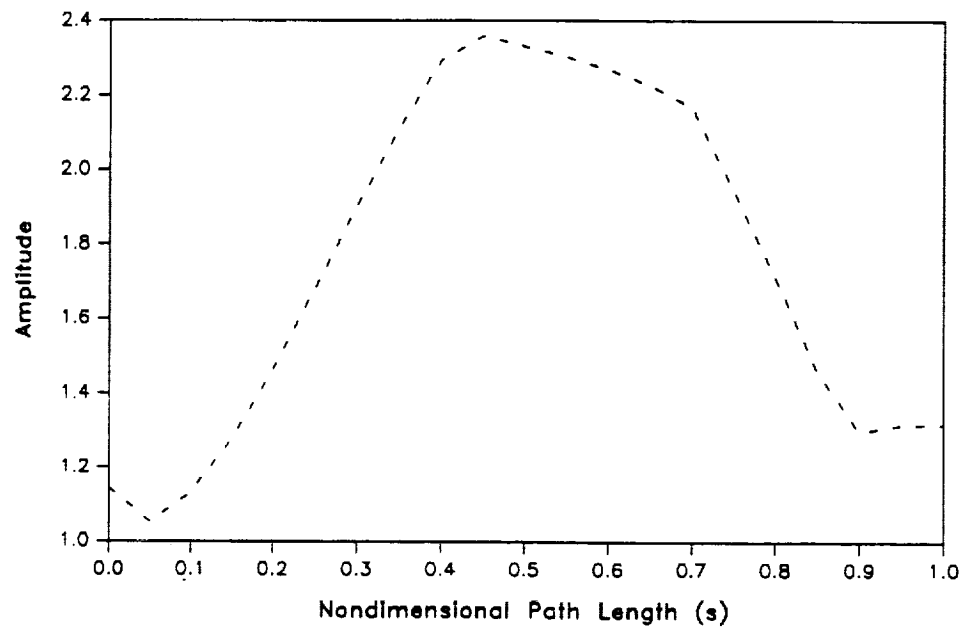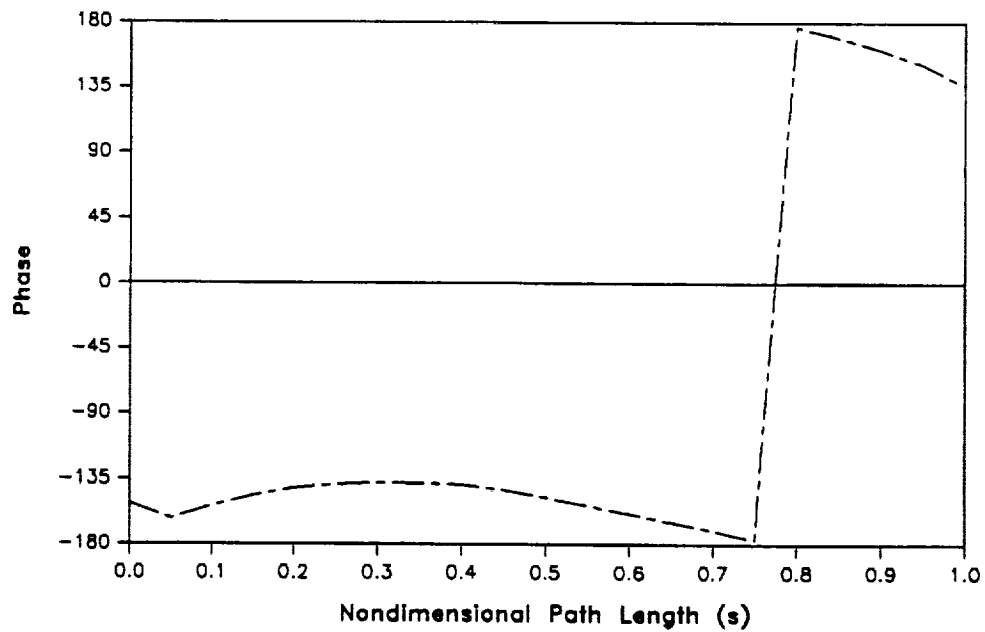## Mode Shape

Phase Plot

Figure 13 - Amplitude and phase plot for precessional excitation for path velocity u_{sl} of compressible model at $f = 0.8$ and $u_{\theta 0}(0) = 0.7$

Noticeable effects of compressibility upon the model can be seen at higher nondimensional frequency ratios. Figure 14 shows the response curves of the compressible and incompressible models for high frequency ratios. The force responses of the incompressible model continue to grow with increasing f, while the results of the compressible model exhibit peaks corresponding to the natural frequency. This is consistent with classical vibration analysis, with the incompressible model having no natural frequency due to an infinitely high bulk modulus, while the compressible model has a natural frequency corresponding to the compressibility of liquid hydrogen in the model.

6.2 Pressure Excitation

This part of the research involves introducing a time and circumferentially varying impeller discharge pressure to the compressible model. With different excitations involved in this model, new boundary conditions also exist. The pressure perturbation takes the form of the following equation.

- *Supply Pressure-Excitation Perturbation*

$$P_s(\theta,t) = P_{s0} + \epsilon P_{s1}(\theta,t) \qquad (45)$$

The occurrence of epsilon in this equation represents the perturbation coefficient for discharge-pressure excitation.

6.2.1 First-Order Equations

Nondimensionalization and perturbation of the general governing equations (6-8) yields the same governing equations for pressure excitation perturbation as for precession excitation governing Eqs. (31-33), except with $h_1 = 0$ for this model. Therefore, the first-order governing equations for pressure excitation will not be presented in this section.
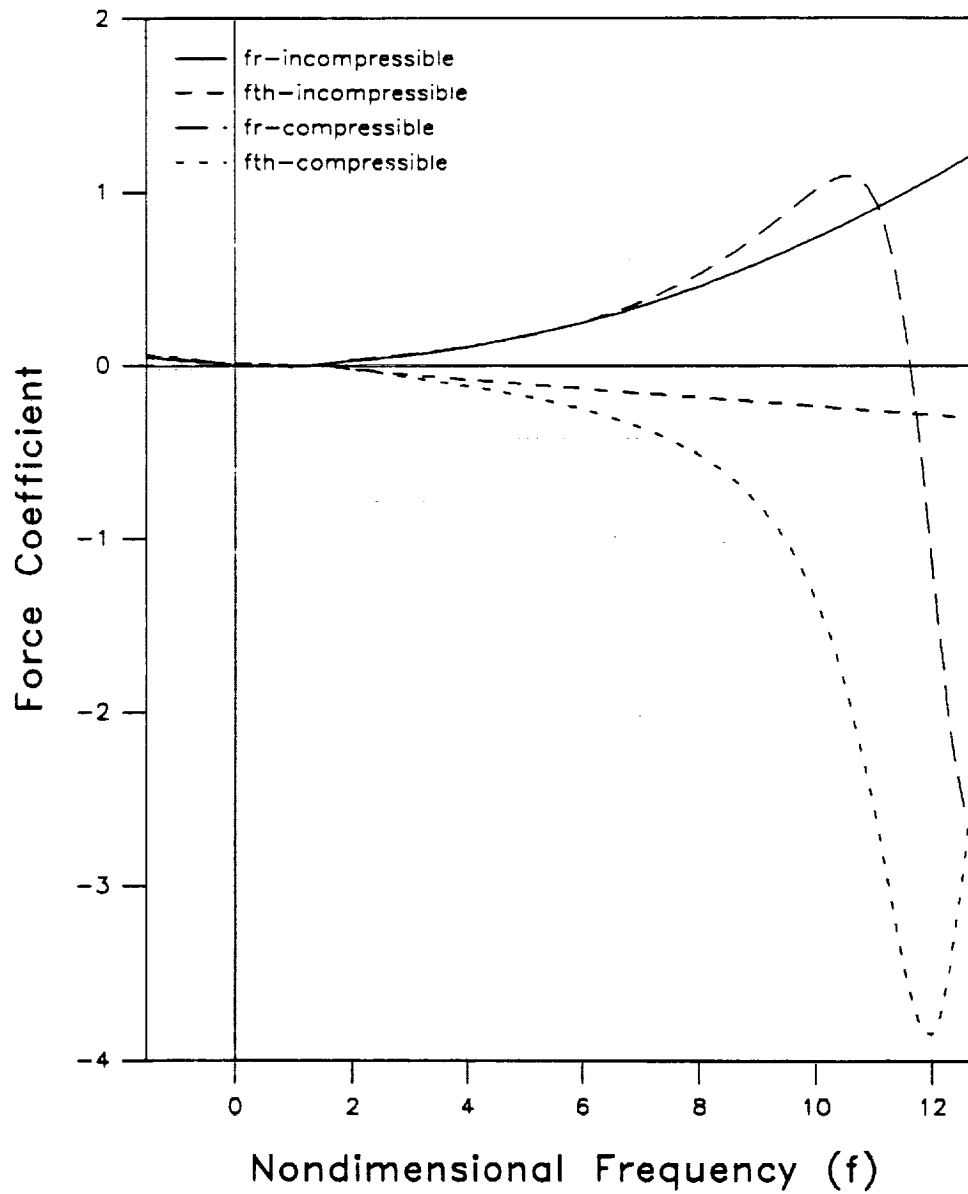
Figure 14 - Nondimensional force response of compressible and incompressible models for precessional excitation for extended frequency range

6.2.2 Boundary Conditions

Nondimensionalization and perturbation of the boundary conditions introduced in Eq. (12-13), the first-order boundary condition can be stated as

$$p_{sI}(\theta,t) - p_1(0,\theta,t) = (1+\xi)u_{sI}(0,\theta,t)\left(1 + \frac{(1+\xi)}{2}\frac{d\bar{\rho}}{dp}|_0\right)$$

$$p_1(1,\theta,t) - p_{eI}(\theta,t) = C_{de}u_{sO}(1)u_{sI}(1,\theta,t)\left(1 + \frac{(1+\xi)}{2}\frac{d\bar{\rho}}{dp}|_1\right)$$

(46)

$p_{sI}(\theta,t)$, $p_{eI}(\theta,t)$ provide the boundary excitations and take the form,

$$p_{sI}(\theta,t) = e^{j\Omega t}(p_{sIc}\cos n\theta + p_{sIs}\sin n\theta)$$
$$p_{eI}(\theta,t) = e^{j\Omega t}(p_{eIc}\cos n\theta + p_{eIs}\sin n\theta)$$

(47)

6.2.3 First Order Solution

The theta and time dependency of the first-order pressure excitation governing equations is eliminated by assuming

$$u_{sI} = e^{jf t}(u_{sIc}\cos n\theta + u_{sIs}\sin n\theta)$$
$$u_{\theta I} = e^{jf t}(u_{\theta Ic}\cos n\theta + u_{sIs}\sin n\theta)$$
$$p_1 = e^{jf t}(p_{Ic}\cos n\theta + p_{Is}\sin n\theta)$$

(48)

where n represents the difference of number of impeller blades and vanes, also defined as the number of diametral nodes (Bolleter). Substitution of Eqs. (48) into the first-order pressure excitation governing equations, equating coefficients of cos $n\theta$ and sin $n\theta$, and using complex variables described in Eq. (30) reduces the real equations to three, complex ordinary differential equations

$$\frac{d}{ds}\begin{Bmatrix}\bar{u}_{sI}\\\bar{u}_{\theta I}\\\bar{p}_1\end{Bmatrix} + [B(n,f,s)]\begin{Bmatrix}\bar{u}_{sI}\\\bar{u}_{\theta I}\\\bar{p}_1\end{Bmatrix} = 0$$

(49)

where

$$[B] = \begin{bmatrix} B_{11} & -\dfrac{jn\omega T}{r} - B_{12} & -\dfrac{d\tilde{\rho}_0}{ds}\left(\dfrac{u_{s0}d\tilde{\rho}_0}{\tilde{\rho}_0^2 ds} + \dfrac{jn\omega T u_{\theta0}}{\tilde{\rho}_0 r}\right) + jn\omega T\dfrac{d\tilde{\rho}_0}{ds} + B_{13} \\[3ex] \dfrac{A_{3s}}{u_{s0}} & \dfrac{A_{2\theta}}{u_{s0}} + \dfrac{jTT}{u_{s0}} & A_{4\theta}\dfrac{d\tilde{\rho}_0}{ds} - j\dfrac{bL_s}{ru_{s0}\tilde{\rho}_0 R_i} \\[3ex] B_{31} & B_{32} & \dfrac{A_{4s}}{\tilde{\rho}_0} - \dfrac{B_{33}}{\tilde{\rho}_0}\dfrac{d\tilde{\rho}_0}{ds} \end{bmatrix} \qquad (50)$$

Eq. (49) differs from Eq. (40) in that Eq. (49) is now a function of n with $h_i = 0$. These equations are solved using the method presented by Childs (1992).

6.2.4 First-Order Results

Results from the pressure excitation perturbation analysis using a difference of impeller blades and vanes (n) is presented in this section. Since the SSME HPFTP wearing-ring seal is located at the end of the leakage path ($s = 1$), the results from this section will concentrate on this area of the leakage path. The pressure-oscillation response at the end of the leakage path versus nondimensional excitation frequency corresponding for $n = 11$ is illustrated in Figure 15. The value of $n = 11$ is used because, as mentioned previously, the SSME HPFTP has 24 impeller blades and 13 diffuser vanes, for a difference of 11. Bolleter (1988) explains that the dominant pressure pattern to be expected for this arrangement would have 11 diametral nodes. This is important because it is the value used as n in Eq. (48). Figure 15 shows that the peak pressure oscillation at the exit of the impeller leakage path ($s = 1$) occurs at a nondimensional frequency of about $f = 6.4$ and $f = 7.8$. Bolleter predicts that the peak pressure oscillation should occur as a function of the difference in the number of impeller blades and vanes, presented in Tables 1 and 2.
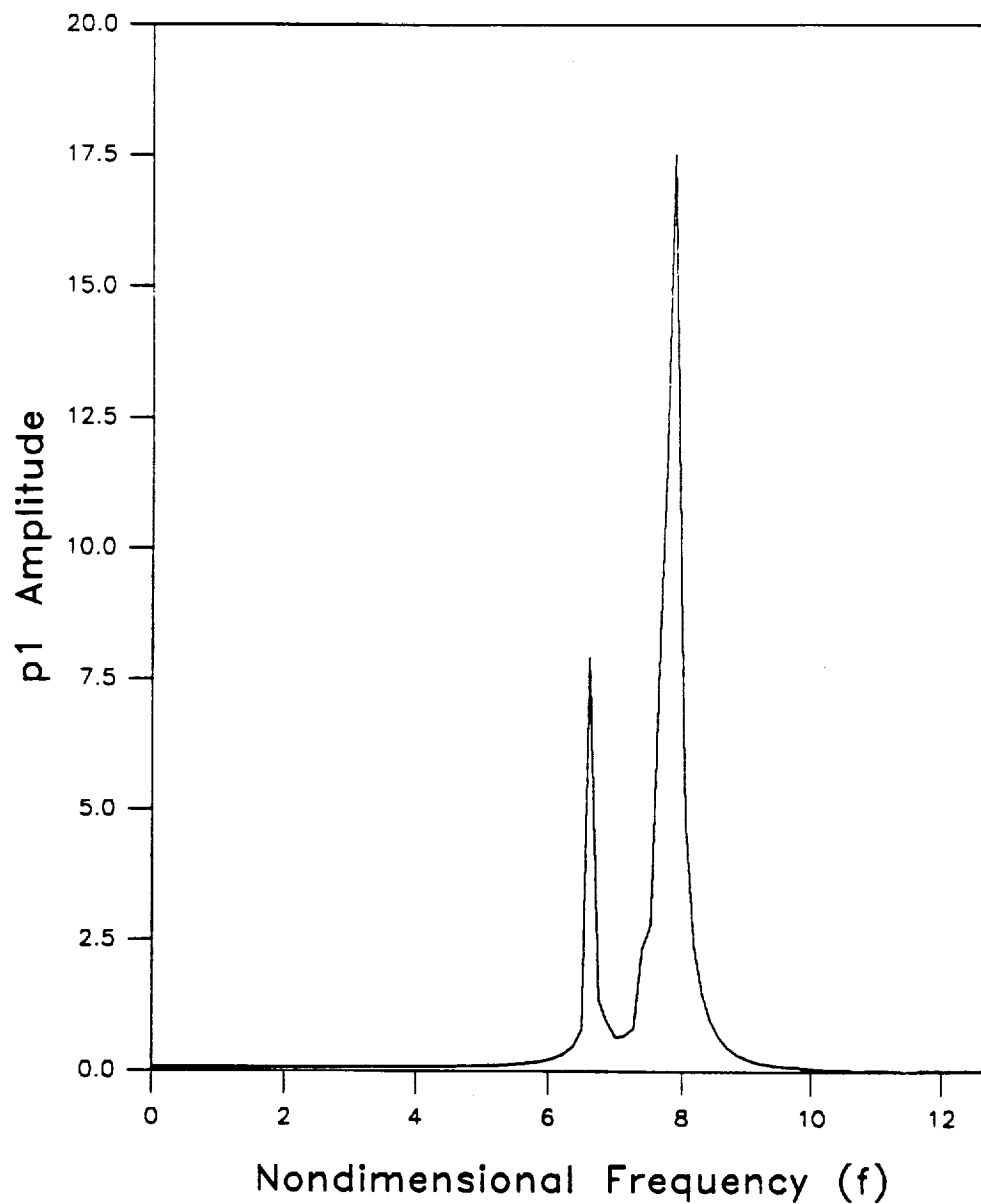
Figure 15 - Pressure oscillation response of compressible model for pressure excitation for $n = 11$ at leakage path exit ($s = 1$) and $u_{to}(0) = 0.7$

The resonant frequency ratios at $f = 6.5$ and $f = 7.8$ clearly are not functions near the predicted excitation frequencies provided in Table 2 for $n = 11$. None of the other cases tested yielded results which correspond to the values shown in Table 2 for the respective value of n. These results reveal that amplification of peak pressure oscillation does not occur at the expected frequency ratio. At the predicted frequency ratios, the cases tested for this model showed that an attenuation, rather than an amplification of the pressure waves occurred.

Table 1 - $(n_1 - n_2)$ for various combinations of multiples of impeller blades and vanes

n_2 \ n_1	24	48	96
13	11	35	83
26	-2	22	70
39	-15	9	57

Table 2 - Expected peak nondimensional frequency ratios, f or, $\{n/(n_1 - n_2)\}$, for various combinations of multiples of impeller blades and vanes

n_2 \ n_1	24	48	96
13	2.18	1.37	1.16
26	-12.00	2.18	1.37
39	-1.60	5.33	1.68

Amplitude and phase plots (Figures 16 and 17) of the pressure oscillation for the two resonant frequency ratios found for n for the compressible pressure excitation model show that the peak pressure oscillation occurs at the exit of the leakage path. This result helps to support the hypothesis that pressure oscillations at the leakage path

Mode Shape
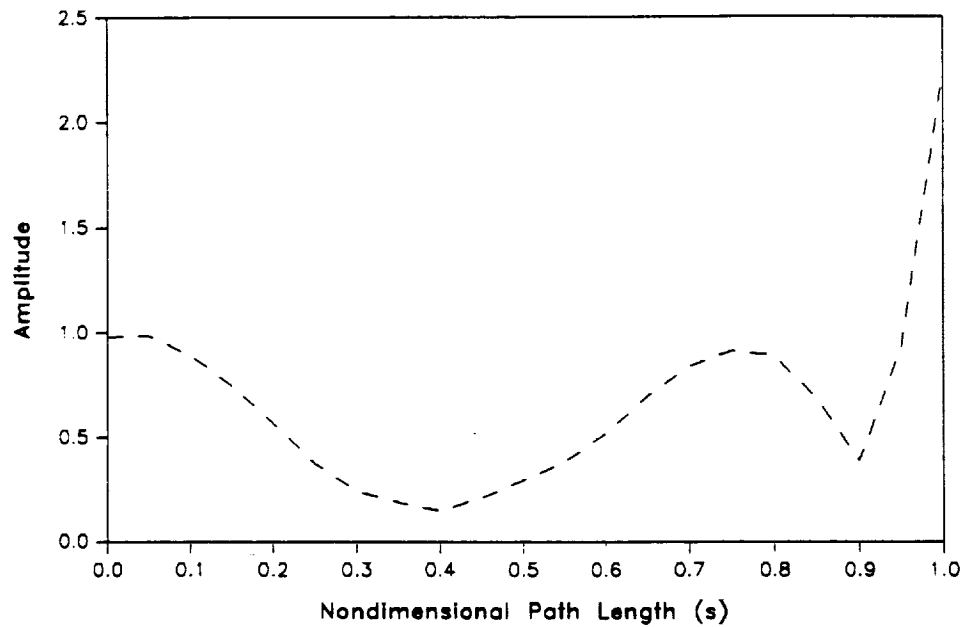
Phase Plot

Figure 16 - Amplitude and phase plot for pressure oscillation of compressible model inside impeller leakage path at $f = 6.4$ for $n = 11$ and $u_{\theta o}(0) = 0.7$

Mode Shape
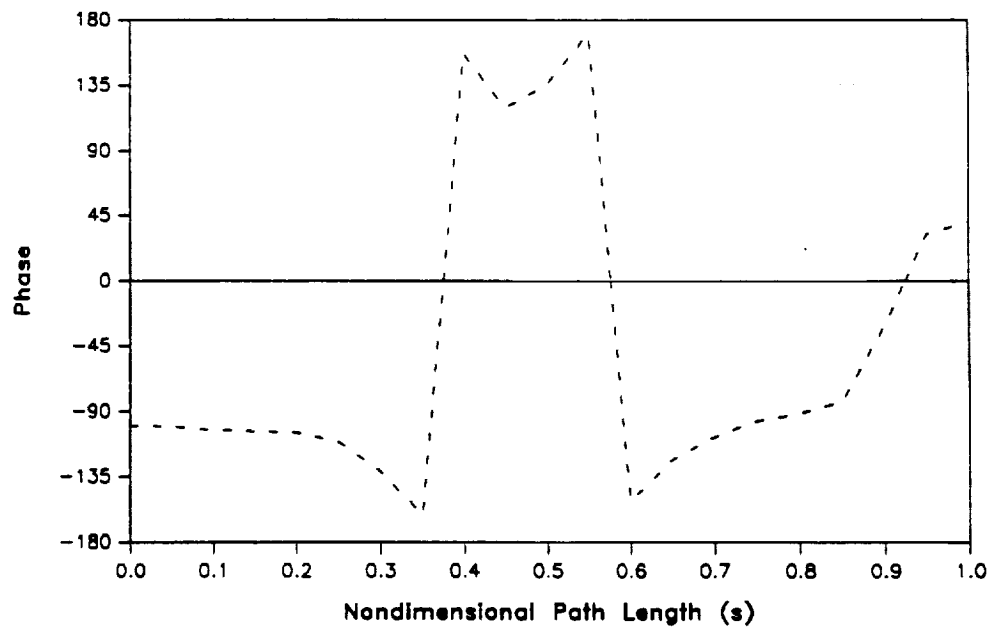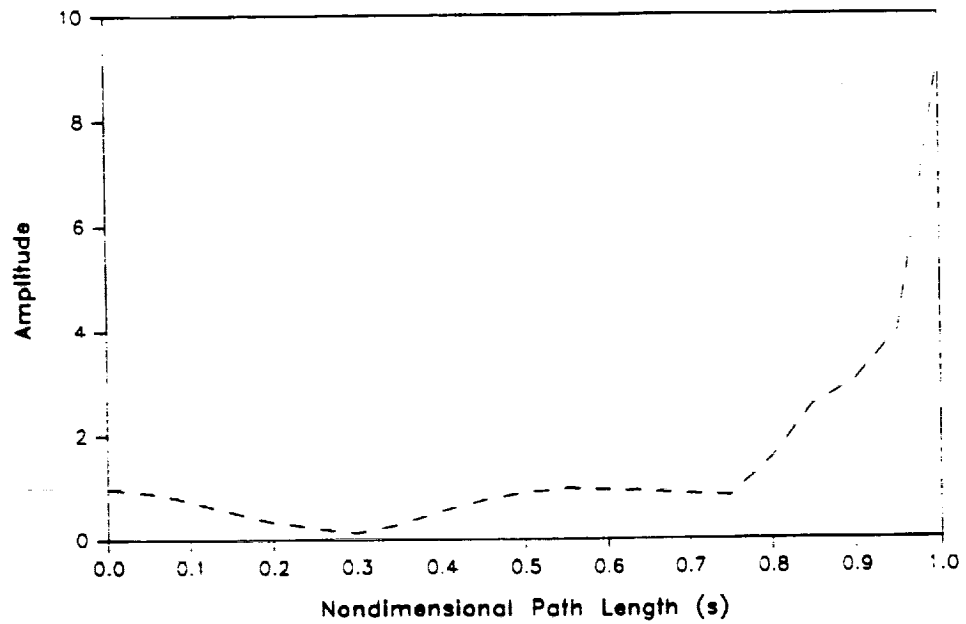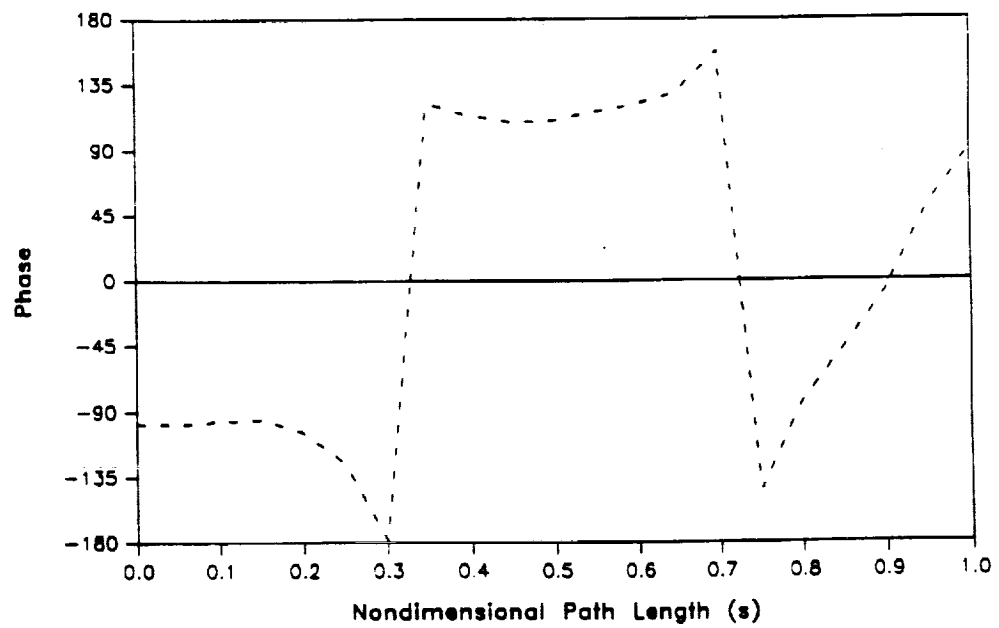

Phase Plot

Figure 17 - Amplitude and phase plot for pressure oscillation of compressible model inside impeller leakage path at $f = 7.5$ for $n = 11$ and $u_\theta(0) = 0.7$

exit are causing the seal to melt. However, the result does not provide enough evidence to provide a very plausible explanation for the behavior exhibited by the wearing ring seal.

The response of the compressible model for other values of n is plotted in Figure 18. The graph shows the relationship of the peak pressure oscillation response to the number of diametral nodes. The nondimensional excitation frequency ratio at which the peak pressure oscillation occurs increases as the number of diametral nodes increase, consistent with Childs' analysis (1992). However, unlike Childs' results, where the magnitude of the peak amplitude stays relatively constant, regardless of n, the results produced from the compressible model show that the amplitude of the pressure oscillations increases as n increases. The effects of added compressibility to the results of this model is greatly enhanced compared to results of the precession excitation model. But, as with the precession excitation analysis, the influence due to compressibility effects is only noticeable at higher nondimensional frequencies.
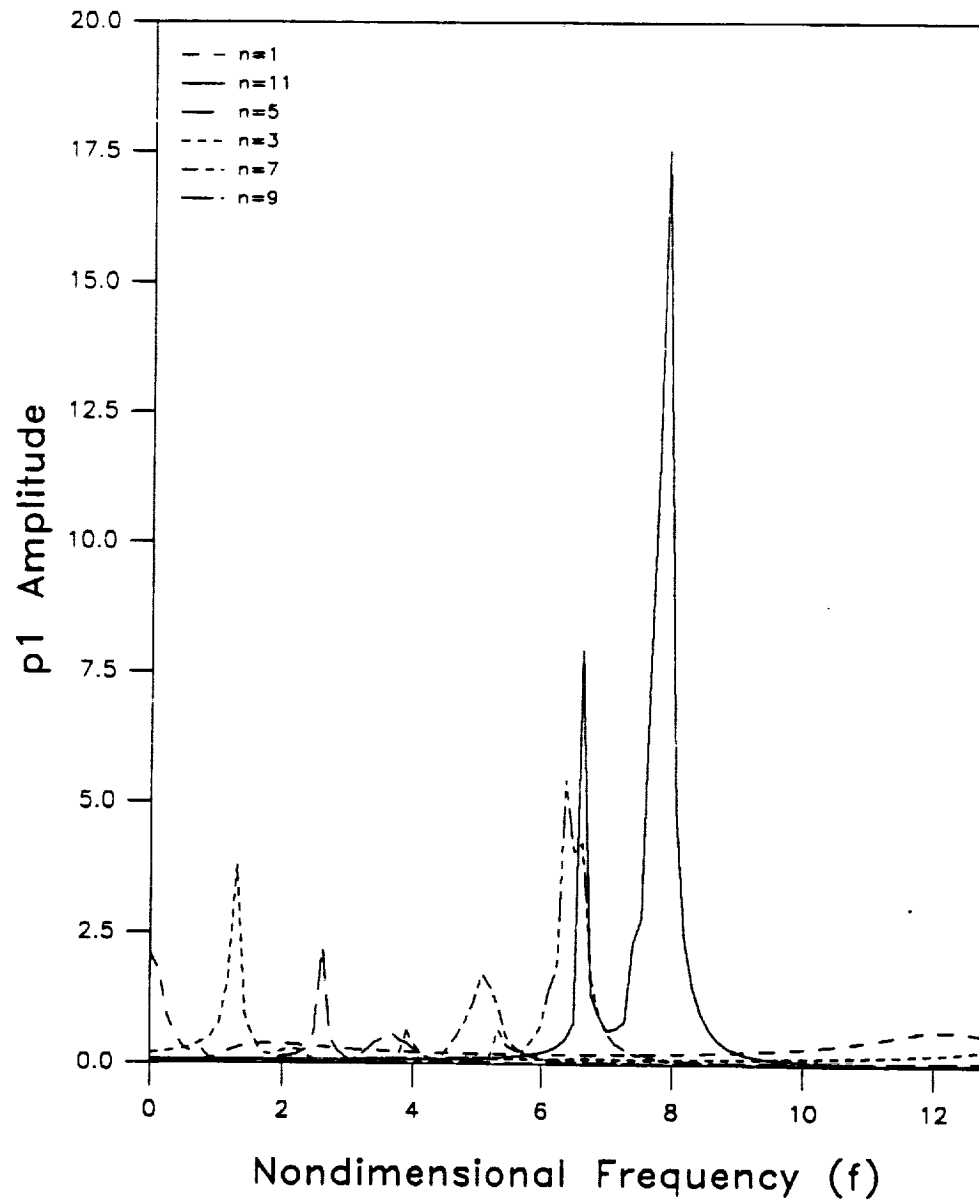
Figure 18 - Pressure oscillation response for pressure oscillation of compressible model with multiple n and $u_{\theta o}(0) = 0.7$

CHAPTER VII
FIRST ORDER EQUATIONS AND SOLUTIONS FOR ACOUSTIC MODELS

For acoustics analysis, the temporal acceleration terms are the only acceleration terms which remain from the set of general governing equations. A highly reasonable assumption may be made that the contributions from the convective, Coriolis, and centrifugal acceleration terms are negligible compared to the temporal acceleration terms in the realm of ordinary acoustics ($M^2 \ll 1$) (Thompson, 1988). However, due to the high Mach number with which the working fluid in the SSME HPFTP operates ($M \cong 0.4$), the general perturbation fluid model and the acoustic model must be compared to investigate the effects of the convective, Coriolis, and centrifugal acceleration terms in an acoustic analysis.

The zeroth-order solution for the acoustics models do not change from the previous results obtained because the zeroth-order equations and solution remain the same .

7.1 Precession Excitation Model

7.1.1 First Order Equations

First-order governing equations for the acoustic precession excitation model can be obtained by removing the effects of fluid mechanics, i.e., the convective, the Coriolis, and the centrifugal acceleration terms from the general perturbation governing equations given in 5.2.2, Eqs. (24-26). Removing the convective acceleration terms, $u_\theta du_\theta/ds$ $u_s du_s/ds$, the Coriolis acceleration term, $2u_{s_0} dr/rds$, and $-2u_{\theta_0} dr/(b^2 rds)$, representing centrifugal acceleration, from the continuity Eq. (24) yields the first-order governing acoustic continuity governing Eq. (51). The first-order governing acoustic equations for the path and circumferential momentum are obtained by removing the convective acceleration terms from Eqs. (25-26).

- *Continuity Equation*

$$\bar{\rho}_0 \frac{\partial h_1}{\partial \tau} + h_0 \frac{\partial \bar{\rho}_1}{\partial \tau} + \frac{1}{T\omega}\left[h_1 \frac{\partial(\bar{\rho}_0 u_{s0})}{\partial s} + u_{s1}\frac{\partial(\bar{\rho}_0 h_0)}{\partial s} + \bar{\rho}_1 \frac{\partial(u_{s0}h_0)}{\partial s}\right] = 0 \qquad (51)$$

- *Path-Momentum Equation*

$$\frac{1}{\bar{\rho}_0}\frac{\partial p_1}{\partial s} + u_{\theta 1}A_{2s} + u_{s1}A_{3s} + \bar{\rho}_1 A_{4s} + T\omega \frac{\partial u_{s1}}{\partial \tau} = h_1 A_{1s} \qquad (52)$$

- *Circumferential-Momentum Equation*

$$\frac{b}{r}\frac{L_s}{R_i \bar{\rho}_0}\frac{\partial p_1}{\partial \theta} + u_{\theta 1}A_{2\theta} + u_{s1}A_{3\theta} + \bar{\rho}_1 A_{4\theta} + T\omega \frac{\partial u_{\theta 1}}{\partial \tau} = h_1 A_{1\theta} \qquad (53)$$

7.1.2 First-Order Precession Excitation Solution

The theta dependency of Eqs. (51-53) can be eliminated by substituting the solution format presented in Eq. (29). The three resulting complex equations in the independent variables s and τ after introducing the complex variables of Eq. (32) are

- *Continuity Equation*

$$
\begin{aligned}
\frac{\partial u_{s1}}{\partial s} &- \frac{j\omega T}{r}u_{\theta 1} + u_{s1}\left[\frac{1}{h_0}\frac{\partial h_0}{\partial s} + \frac{1}{\bar{\rho}_0}\frac{\partial \bar{\rho}_0}{\partial s}\right] = h_1\left[\frac{u_{s0}}{h_0^{2}}\frac{\partial h_0}{\partial s} + j\frac{\omega T}{h_0 r}u_{\theta 0}\right] \\
&+ \bar{\rho}_1\left[j\frac{\omega T}{\bar{\rho}_0 r}u_{\theta 0} + \frac{u_{s0}}{\bar{\rho}_0^{2}}\frac{\partial \bar{\rho}_0}{\partial s}\right] - \frac{\omega T}{h_0}\frac{\partial h_1}{\partial \tau} - \frac{u_{s0}}{h_0}\frac{\partial h_1}{\partial s} - \frac{\omega T}{\bar{\rho}_0}\frac{d\bar{\rho}_1}{dp_1}\frac{\partial p_1}{\partial \tau}
\end{aligned} \qquad (54)
$$

- *Path-Momentum Equation*

$$\frac{\partial p_1}{\bar{\rho}_0 \partial s} + u_{\theta 1}A_{2s} + u_{s1}A_{3s} + \bar{\rho}_1 A_{4s} + T\omega \frac{\partial u_{s1}}{\partial \tau} = h_1 A_{1s} \qquad (55)$$

- *Circumferential-Momentum Equation*

$$-\frac{b}{r}\frac{L_s}{R_i}\frac{p_1}{\tilde{\rho}_0} + u_{\theta 1}A_{2\theta} + u_{sf}A_{3\theta} + \tilde{\rho}_1A_{4\theta} + T\omega\frac{\partial u_{\theta 1}}{\partial \tau} = h_1 A_{1\theta} \qquad (56)$$

Assuming the harmonic seal motion described in section 6.1, Eq. (38), the three governing equations reduce to two differential equations of motion of the form,

$$\frac{d}{ds}\begin{Bmatrix} u_{sl} \\ p_1 \end{Bmatrix} + [C]\begin{Bmatrix} u_{sl} \\ p_1 \end{Bmatrix} = \left(\frac{q_0}{\epsilon}\right)\begin{Bmatrix} g_7 \\ g_8 \end{Bmatrix} \qquad (57)$$

where

$$\begin{Bmatrix} g_7 \\ g_8 \end{Bmatrix} = \left(\frac{L}{L_s}\right)\begin{Bmatrix} \dfrac{u_{s0}}{\tilde{\rho}_0}\dfrac{d\tilde{\rho}_0}{dp}G_q + F_2 + j\dfrac{\Gamma T}{h_0}\dfrac{dz}{ds} - j\dfrac{\omega T}{r}\dfrac{A_{1\theta}}{(A_{2\theta} + j\omega Tf)} \\[4mm] G_q - \dfrac{A_2 A_{1\theta}}{(A_{2\theta} + j\omega Tf)} \end{Bmatrix} \qquad (58)$$

The [C] matrix elements are given in Appendix C.

The $du_{\theta 1}/ds$ term has dropped from the governing equations and thus $u_{\theta 1}$ can be solved directly without integrating the partial differential equations, yielding,

$$u_{\theta 1} = \left[h_1 A_{1\theta} - u_{sf}A_{3\theta} + \left(j\frac{b}{r}\frac{L_s}{R_i\tilde{\rho}_0} - \frac{d\tilde{\rho}_0}{dp}A_{4\theta}\right)p_1\right] / (A_{2\theta} + j\omega Tf) \qquad (59)$$

Results to these equations are obtained using the same solution procedure and boundary conditions described for the first-order precession excitation equations in section 6.2.2. The solution to these sets of equations can then be used to calculate the force and moment coefficients in the impeller leakage path for the acoustic case where classical acoustic assumptions are made.

C-2

7.1.3 First-Order Results

The nondimensional radial force coefficient responses for the general perturbation and acoustic cases are shown in Figure 19. The response curves for the circumferential force coefficients are shown in Figure 20. The response curves for the acoustic case are less erratic in behavior, and the peaks exhibited by the compressible model totally disappear. This shows that the convective, Coriolis, and centrifugal acceleration terms do affect the results of the compressible model to a considerable extent at low frequencies. Childs (1989) correctly predicted that the centrifugal acceleration terms caused the resonance in the response curve. Although the results of the two models do not differ quantitatively, the trend exhibited by both models are similar, as evidenced by Figures 20 and 21.

At higher values of nondimensional frequency, the effects of removing the fluid mechanics terms from the model is shown in Figure (21). The two models show about the same results. The natural frequency of the acoustic model is slightly lower and the peaks are slightly higher. Mode shapes for pressure oscillations at $f = 11.5$ and $f = 12$ are shown in Figures 22 and 23. The mode shapes show that, at these frequencies, the pressure oscillations are not the cause of the uncharacteristic behavior of the exit wearing ring seal due to a precession excitation. The mode shapes do not show conclusively that the pressure oscillations are occurring at the exit of the seal.

7.2 Pressure Excitation Model

7.2.1 First-Order Equations

The equations obtained for the first-order acoustic pressure excitation perturbation use the same procedure as for the first-order acoustic precession excitation shown in section 7.1.1. The boundary conditions and perturbation excitation are defined by the equations used for the general first-order pressure excitation solution given in section 6.2. The resulting governing equations for pressure excitation of the acoustic model are the same as those given in section 7.1.1, except with h_l being zero, analogous with the results obtained for the pressure excitation equations for the general perturbation model.
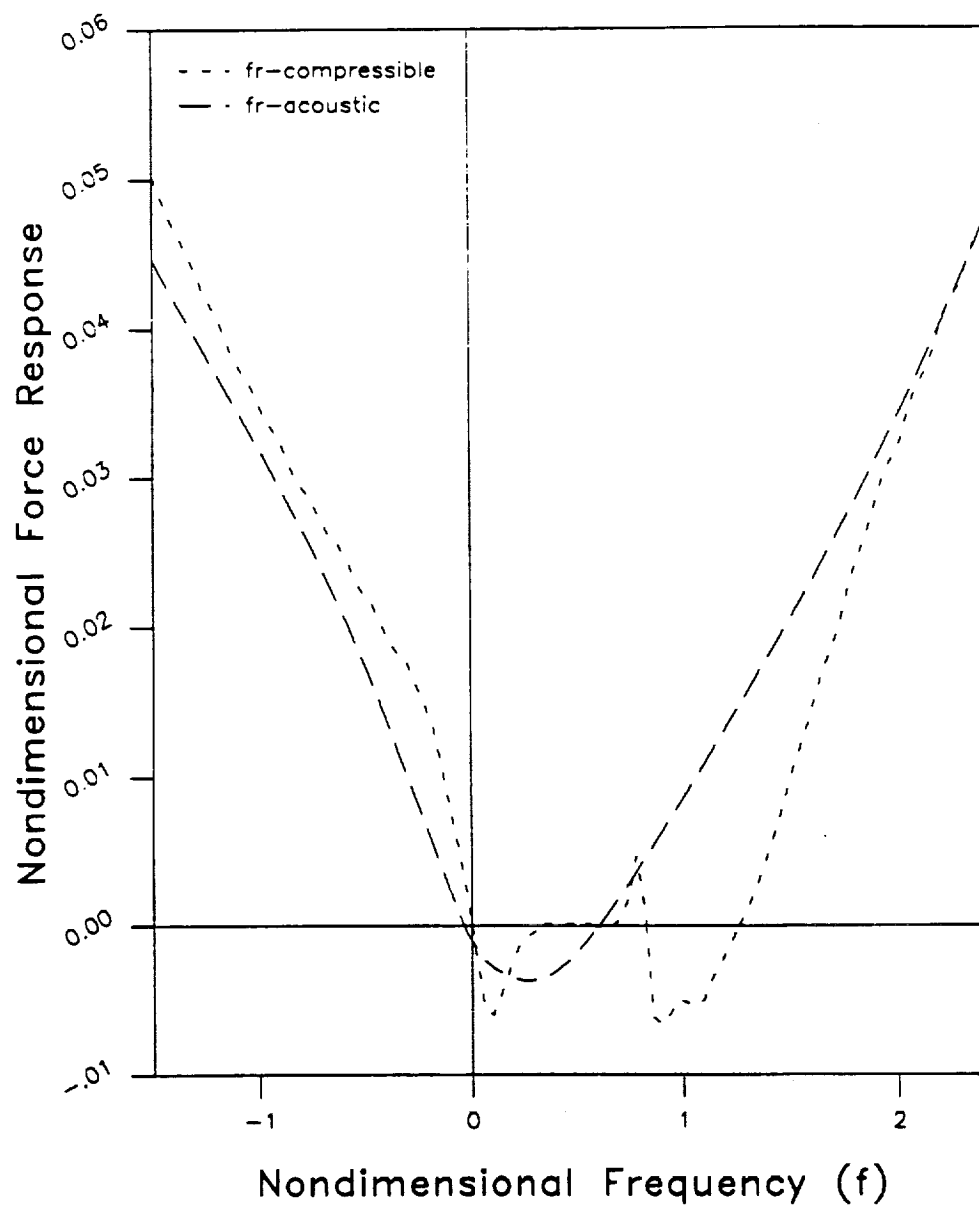
Figure 19 - Radial response for acoustic and compressible models for precessional excitation for $u_{\theta o}(0) = 0.7$
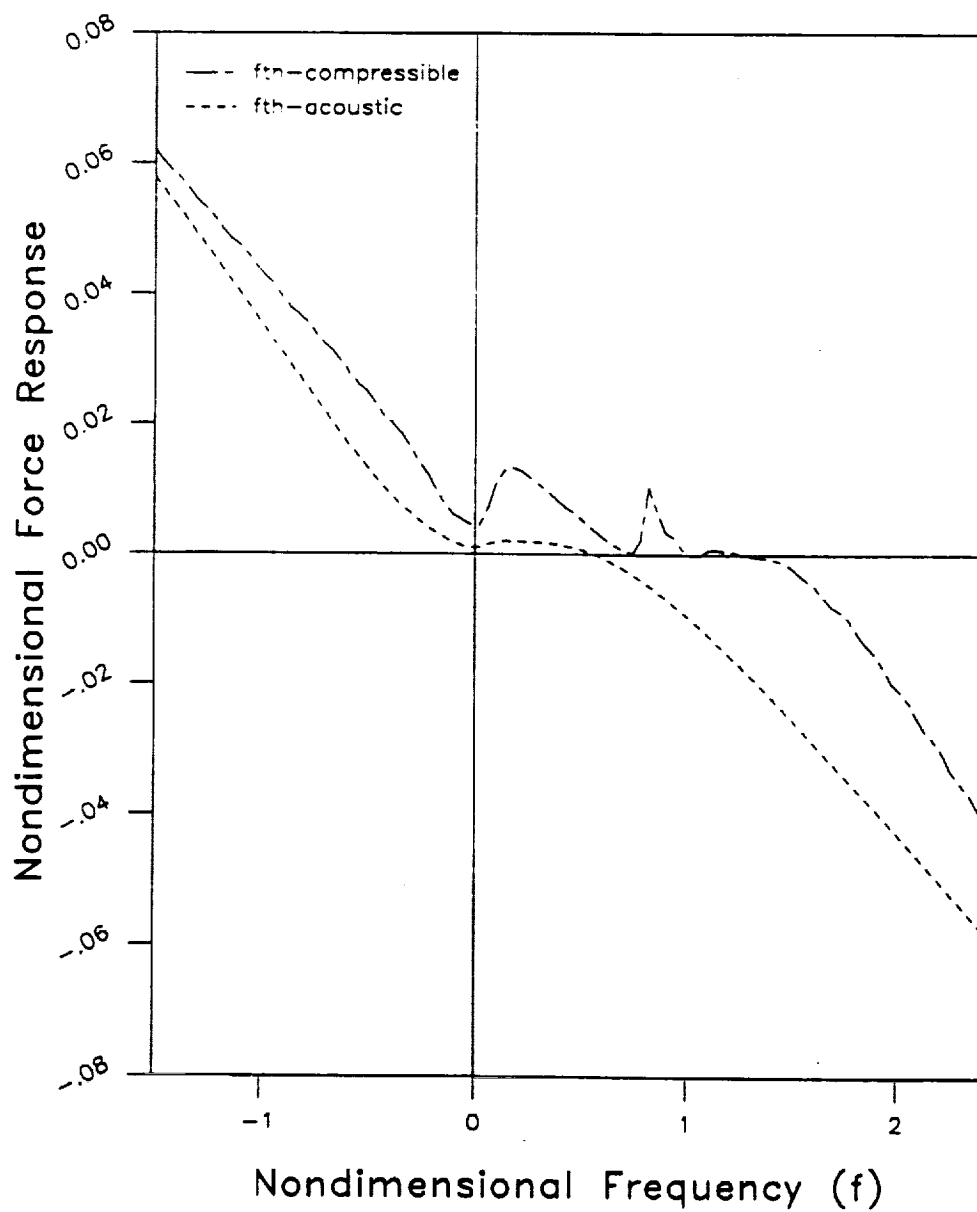
Figure 20 - Circumferential force response for acoustic and compressible models for precessional excitation for $u_{\theta 0}(0) = 0.7$
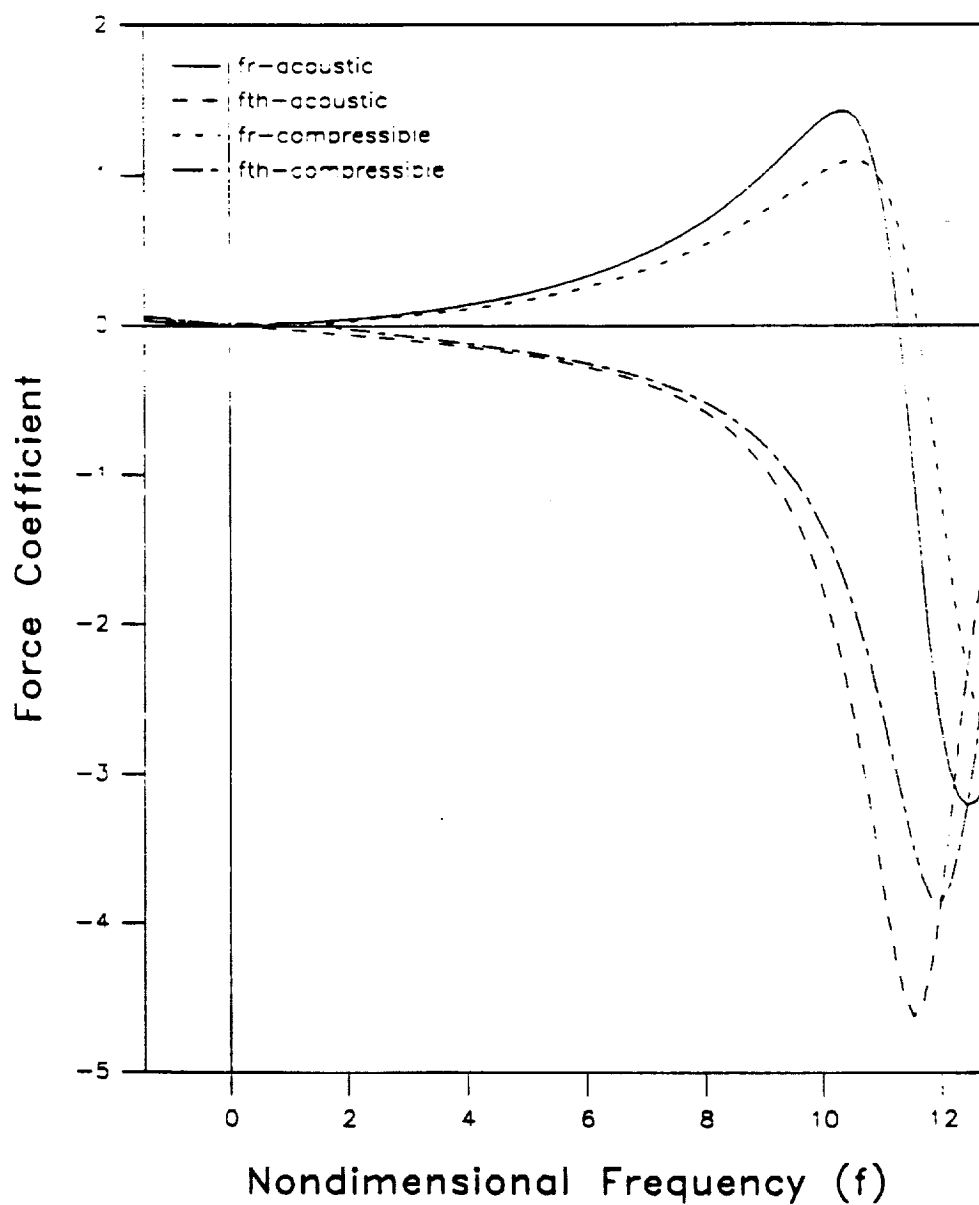
Figure 21 - Force response coefficient for acoustic and compressible models at extended frequency ratios

Mode Shape
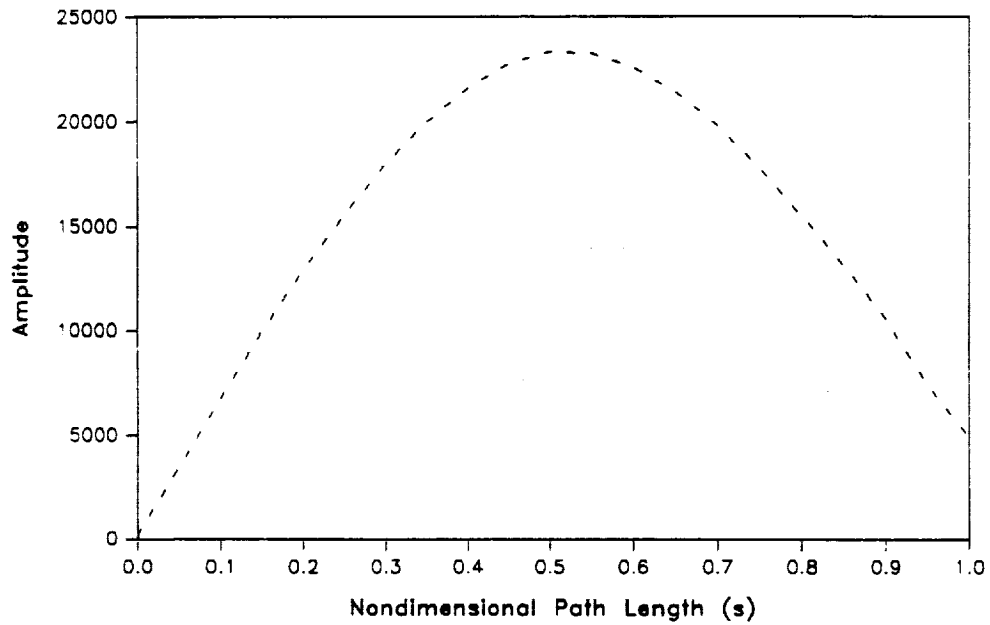
Phase Plot
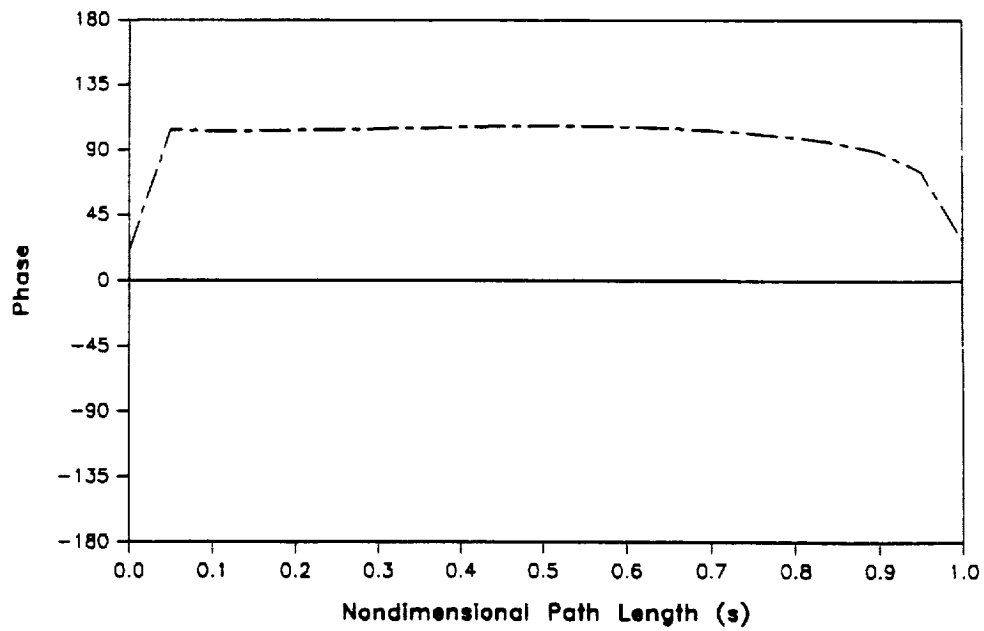
Figure 22 - Amplitude and phase plot of nondimensional pressure of acoustic model vs. path length at $f = 11.5$ for $u_{\theta\theta}(0) = 0.7$

Mode Shape

Phase Plot

Figure 23 - Pressure mode shape and phase plot of acoustic model vs. path length at $f = 12.0$ for $u_\theta(0) = 0.7$

Figure 24 - Acoustic response for impeller discharge pressure excitation for $n = 11$ for $u_{\theta 0}(0) = 0.7$

7.2.2 First-Order Pressure Excitation Solution

Using Eq. (48) to eliminate the theta and time dependency from the first-order pressure excitation of the acoustic model and using the pressure excitation perturbation described in Eq. (45), the resulting governing equations can be represented as,
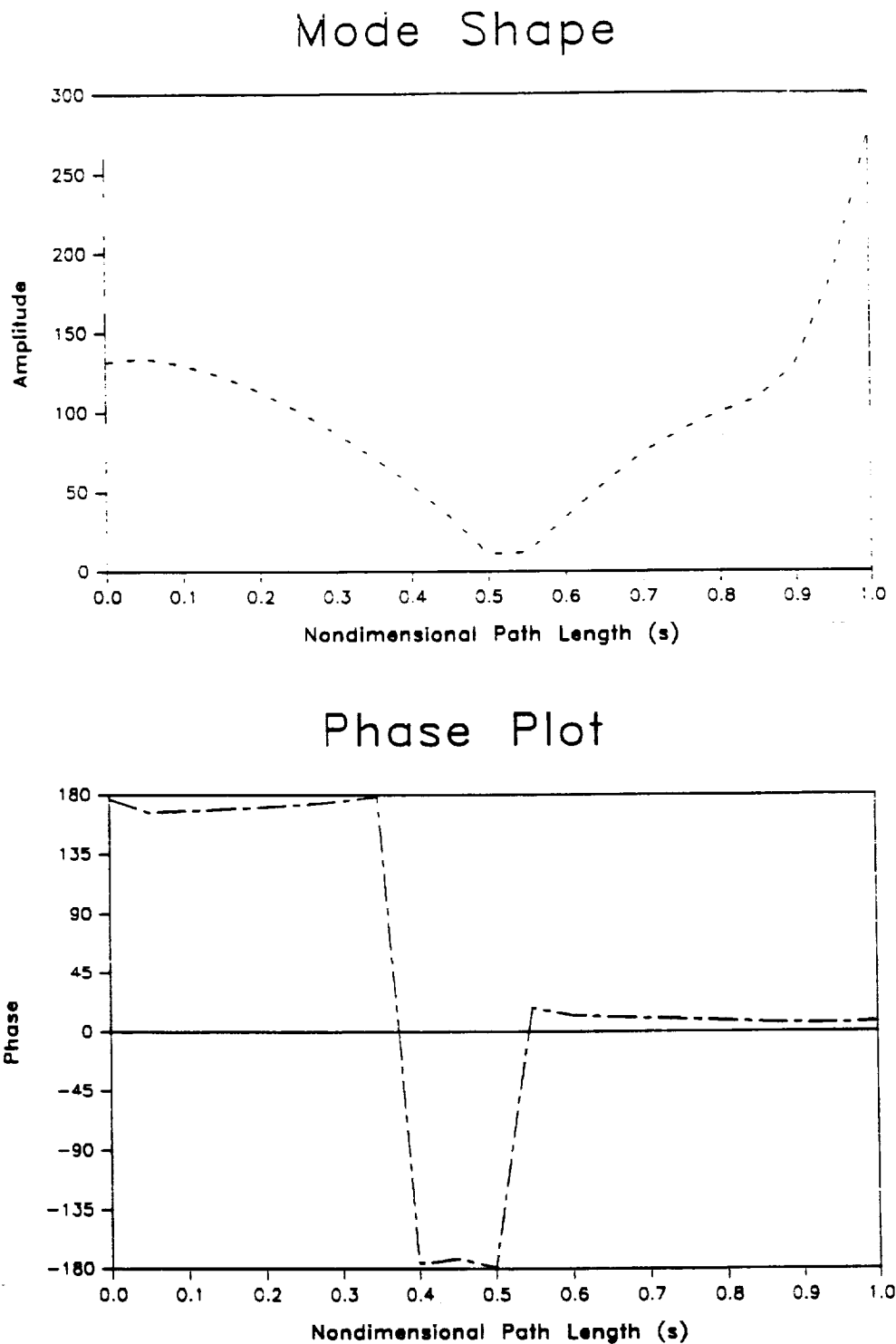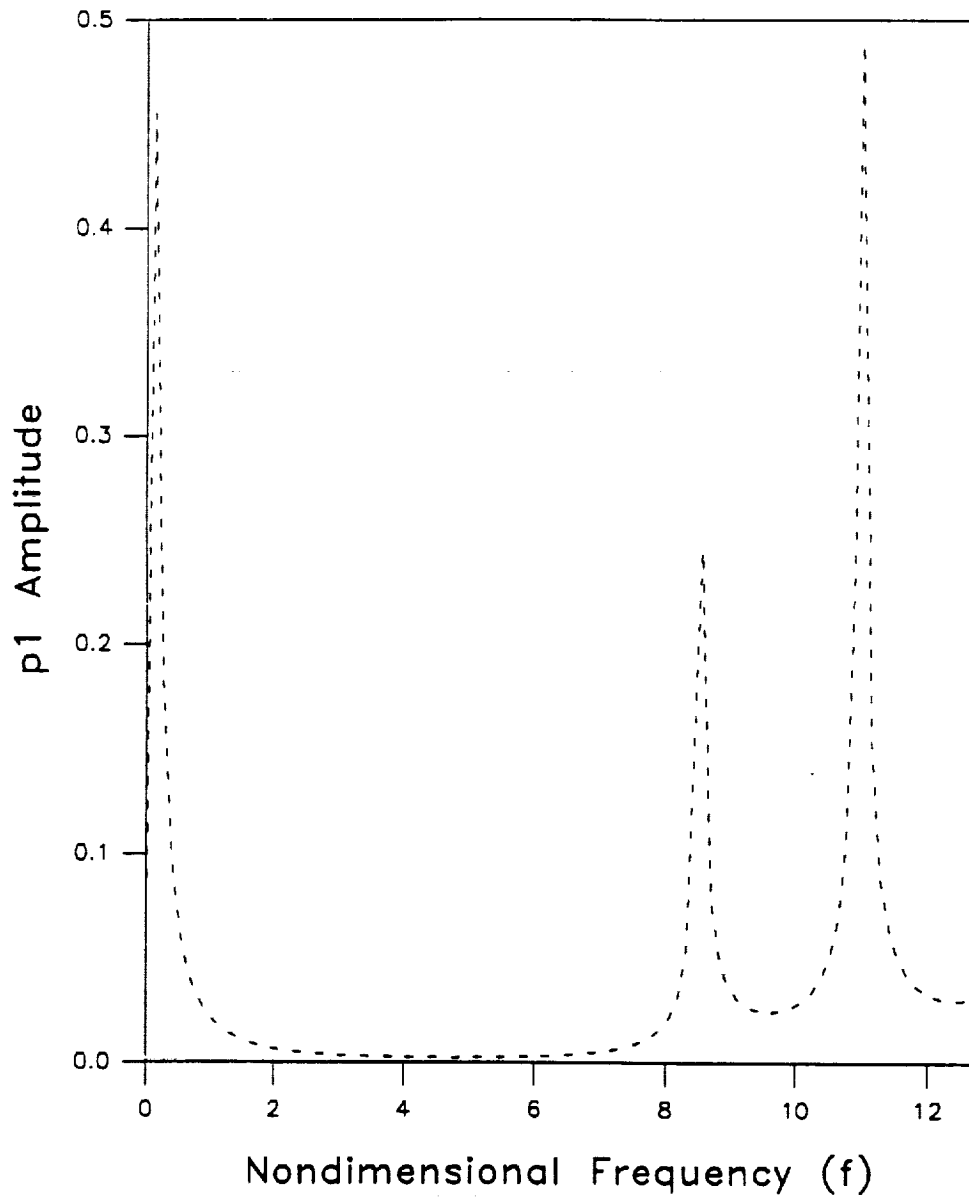
$$\frac{d}{ds}\begin{Bmatrix} u_{sl} \\ p_1 \end{Bmatrix} + [D]\begin{Bmatrix} u_{sl} \\ p_1 \end{Bmatrix} = 0 \tag{60}$$

Where elements of [D] are provided in Appendix D.

In addition to h_1 being zero, Eq. (60) also is a function of n, unlike Eq. (57).

7.2.3 First-Order Results

Comparison of the general perturbation model and the acoustic model for $n = 11$ shows that the peak pressure amplification around $f = 7.8$ displayed by the general perturbation model almost totally disappears for the acoustics model. From Figure 24, the results for the acoustics model show that no amplification of the pressure oscillation occurs, but rather, an attenuation of the pressure oscillation at all frequency ratios. It can be concluded from this result that the convective, Coriolis, and centrifugal acceleration terms contribute significantly to the results of a bulk flow model when a pressure excitation is used as the perturbation parameter of the bulk flow model. The results here also differ with respect to the location of the resonant peaks in the nondimensional frequency range tested. For the acoustic model, the local peaks do not match with those of the compressible model.

The sharp peak of the pressure amplitude near a frequency ratio of $f = 0.0$ is inherent in all the models (compressible, incompressible, and acoustic), shown in Figure 25. The phenomenon causing this resonant excitation is not yet understood and cannot be explained. However, the fact that this resonance occurs in all three models explains that neither the compressibility or the acoustics effects of the models affects this resonant frequency. Also, the fact that the frequency at which resonance occurs is near $f = 0.0$, indicates that this peak could be the response to a free vibration of

the fluid inside the leakage path.

Figure 26 shows the first-order pressure response for multiple cases of n. The frequency responses due to different n show no quantitative trend with respect to n. Unlike the compressible model, where the pressure response showed a definite, noticeable response to different n, the acoustic model shows little quantitative and qualitative response to different n value.
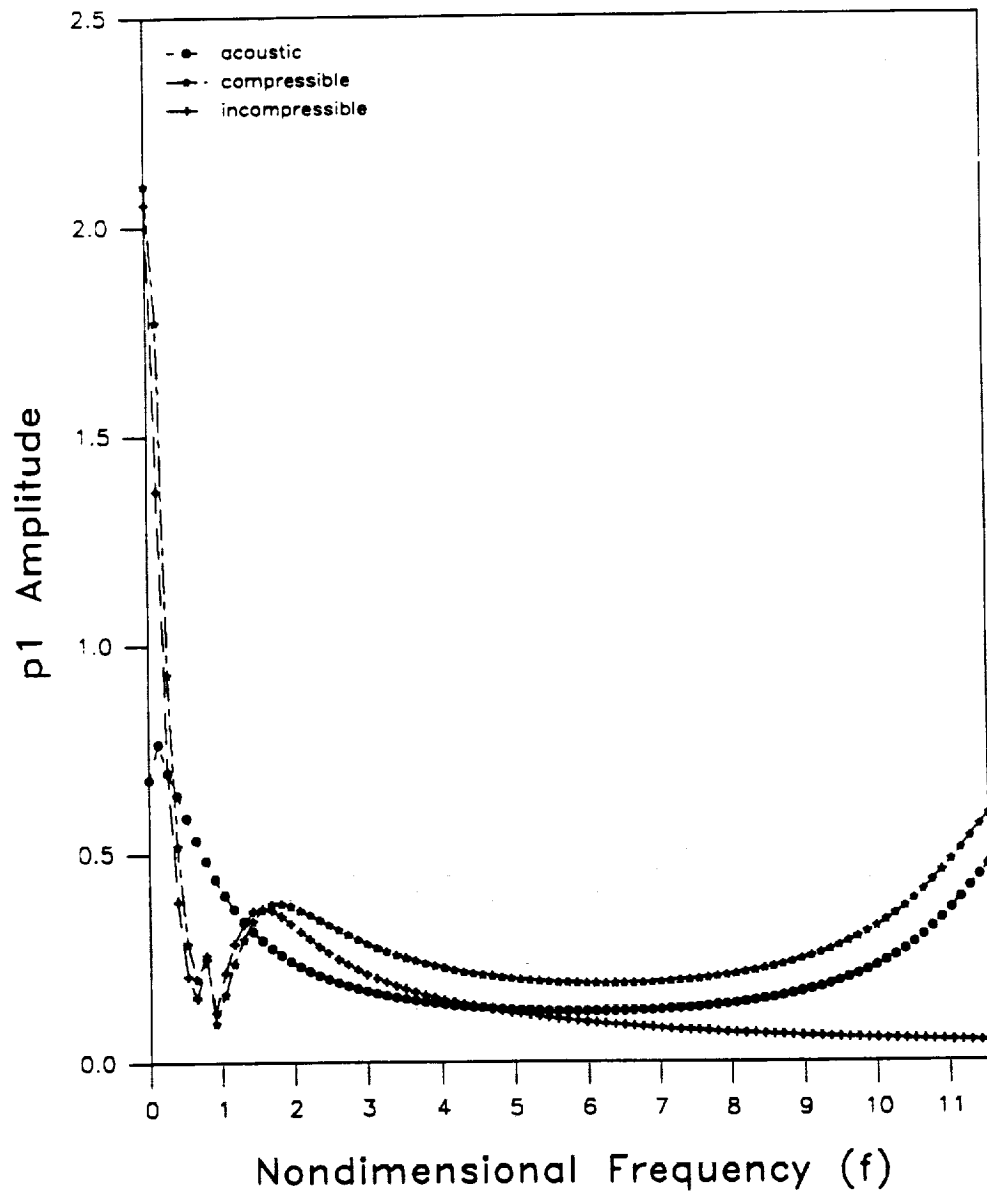
Figure 25 - Pressure response of incompressible, compressible, and acoustic model for impeller discharge pressure excitation for $n = 1$ for $u_{\theta 0}(0) = 0.7$
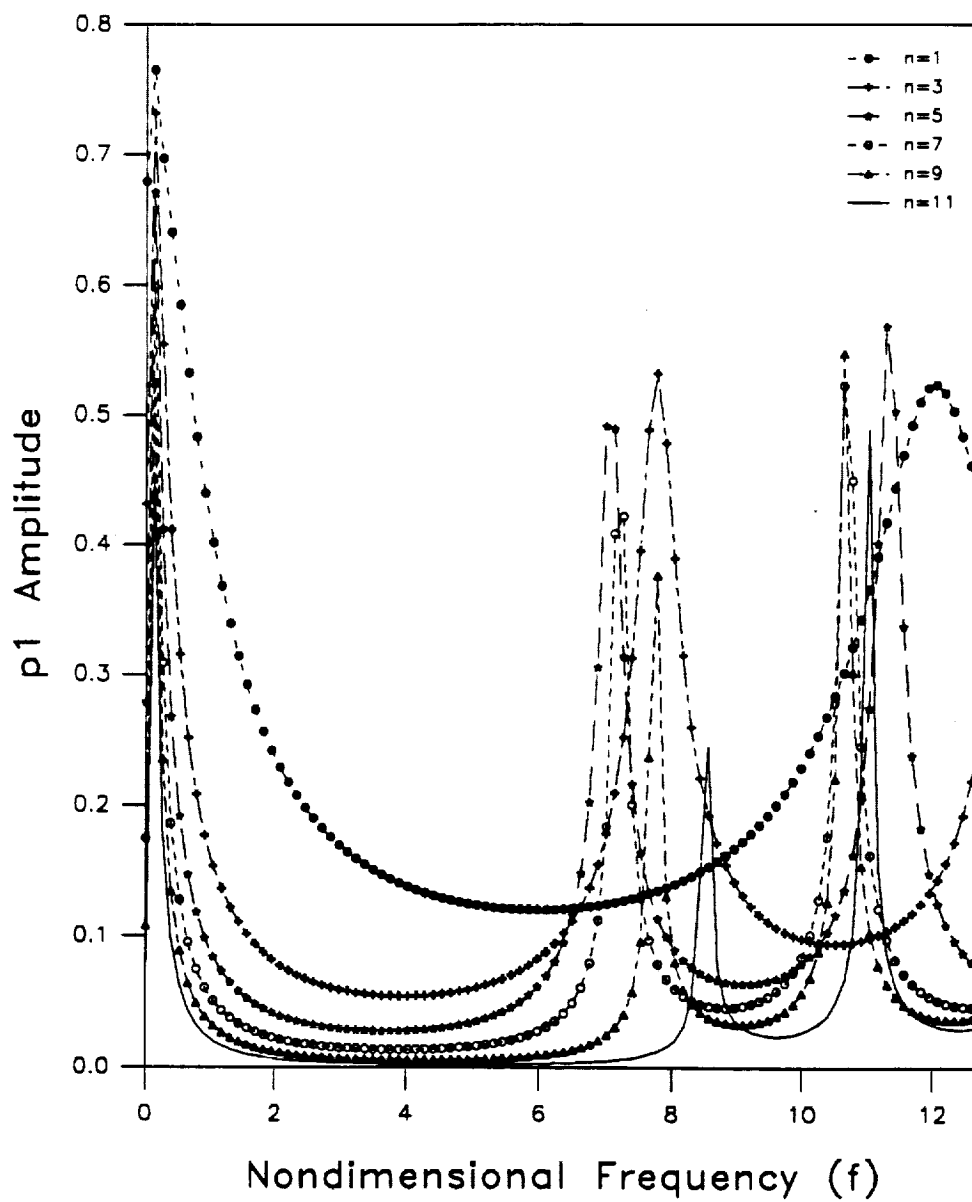
Figure 26 - Pressure response for pressure excitation for multiple *n*

CHAPTER VIII
SUMMARY AND CONCLUSIONS

A modified approach to Childs' previous work (1989,1992) on fluid-structure interaction forces in the leakage path between an impeller shroud and its housing is presented in this thesis. Three governing equations consisting of a continuity, path-momentum, and circumferential-momentum equations were developed to describe the leakage path inside a pump impeller. Radial displacement perturbations were used to solve for radial and circumferential force coefficients. In addition, impeller-discharge pressure disturbances were used to obtain pressure oscillation responses due to precessing impeller pressure wave pattern. Childs' model was modified from an incompressible model to a compressible barotropic-fluid model (the density of the working fluid is a function of the pressure and a constant temperature only). Results obtained from this model yielded interaction forces for radial and circumferential force coefficients. Radial and circumferential forces define reaction forces within the impeller leakage path.

An acoustic model for the same leakage path was also developed. The convective, Coriolis, and centrifugal acceleration terms are removed from the compressible model to obtain the acoustics model. The compressible model is compared with the incompressible model and the acoustic model. A solution due to impeller discharge pressure disturbances model was also developed for the compressible and acoustic models. The results from these modifications are used to determine what effects additional perturbation terms in the compressible model have on the acoustic model.

The results show that the additional fluid mechanics terms in the compressible model do cause resonances (peaks) in the force coefficient response curves. However, these peaks only occurred at high values of inlet circumferential velocity ratios. The peak pressure oscillation was shown to occur at the wearing ring seal. Introduction of impeller discharge disturbances with n diametral nodes showed that maximum peak

pressure oscillations occurred at nondimensional excitation frequencies of $f = 6.4$ and $f = 7.8$ for this particular pump. Bolleter's results suggest that for peak pressure oscillations to occur at the wearing ring seal, the nondimensional excitation frequency should be on the order of $f = 2.182$ for $n = 11$. The resonances found in this research do not match those predicted by Bolleter. At the predicted frequencies given by Bolleter, the compressible model shows an attenuation of the pressure oscillations at the seal exit. This does not provide a plausible explanation for the unusual behavior exhibited by the wearing ring seal.

The compressibility of the fluid does not have a significant influence on the model at low values of nondimensional frequency. At high values of nondimensional frequency, the effects of compressibility become more significant. For the acoustic analysis, the convective, Coriolis, and centrifugal acceleration terms do affect the results to a limited extent for a precession excitation and a large extent for a pressure excitation when the fluid operates at relatively high mach numbers.

REFERENCES

Bolleter, U., 1988, "Blade Passage Tones of Centrifugal Pumps", *Vibrations*, Vol. 4, September, pp. 8-13.

Childs, D. W., 1989, "Fluid-Structure Interaction Forces at Pump-Impeller-Shroud Surface for Rotordynamic Calculations," ASME *Journal of Vibrations, Acoustics, Stress, and Reliability in Design*, Vol. 111, July, pp. 216-225.

Childs, D. W., 1992, "Pressure Oscillations in the Leakage Annulus Between a Shrouded Impeller and Its Housing Due to Impeller-Discharge-Pressure Disturbances," *Journal of Fluids Engineering*, Vol. 114, March, pp. 61-67.

McCarthy, R. D., 1986, "Thermophysical Properties of Fluids, MIPROPS 86," NBS Standard Reference Data Base 12, Thermophysics Division, Center for Chemical Engineering, National Bureau of Standards, Boulder, Colorado.

Morrison, G. L., Rhode, D. L., Logan, K. C., Chi, D., Demco, J., 1983, "Labyrinth Seals for Incompressible Flow - Final Report," G. C. Marshall Space Flight Center, MSFC, Alabama, 35812, Report Number SEAL-4-83, November.

San Andres, L., 1991, "Analysis of Turbulent Hydrostatic Bearings with a Barotropic Fluid," Transactions of the ASME, ASME *Journal of Tribology*, pp. 1-10.

Thompson, P. A., *Compressible Fluid Mechanics*, Department of Mechanical Engineering, Rensselaer Polytechnic Institute, Troy, New York, 1988, pp. 159-163.

Thomson, W. T., *Laplace Transformations*, Prentice Hall, Inc., Englewood Cliffs, New Jersey, 1960, Second Edition, pp.181-201.

APPENDIX A

$$A_{4\theta} = \frac{u_{so}^2}{2h_0\tilde{\rho}_0}\left[\sigma_r(u_{\theta 0} - 1)mr + \sigma_s u_{\theta 0} ms\right]$$

(A.1)

$$A_{4s} = \frac{u_{so}^2}{2h_0\tilde{\rho}_0}(\sigma_r mr + \sigma_s ms)$$

(A.2)

Coefficient definitions for [A] *Eq. (40)*

$$A_{11} = \left[-\tilde{\rho}_0 u_{so}\left(\frac{dh_0}{h_0 ds} + \frac{d\tilde{\rho}_0}{\tilde{\rho}_0 ds} + \frac{dr}{rds}\right) - A_{3s}\tilde{\rho}_0 + j\Gamma T\tilde{\rho}_0\right]u_{so}/\left(\frac{d\tilde{\rho}_0}{dp}\frac{1}{\tilde{\rho}_0} - u_{so}\tilde{\rho}_0\right) + \left(\frac{1}{h_0}\frac{dh_0}{ds} + \frac{1}{\tilde{\rho}_0}\frac{d\tilde{\rho}_0}{ds} + \frac{1}{r}\frac{dr}{ds}\right)$$

(A.3)

$$A_{12} = u_{so}\left[A_{2s}\tilde{\rho}_0 + j\frac{\omega T}{r}\tilde{\rho}_0 u_{so}\right]/\left(\frac{d\tilde{\rho}_0}{dp}\frac{1}{\tilde{\rho}_0} - u_{so}^2\tilde{\rho}_0\right)$$

(A.4)

$$A_{13} = \frac{u_{so}}{\tilde{\rho}_0 F_s}\frac{d\tilde{\rho}_0}{dp}\left[\tilde{\rho}_0 u_{so}\frac{d\tilde{\rho}_0}{dp}\left(\frac{u_{so}}{\tilde{\rho}_0^2}\frac{d\tilde{\rho}_0}{ds} + j\frac{\omega T u_{\theta 0}}{\tilde{\rho}_0 r}\right) - j\omega T u_{so}\tilde{\rho}_0 - A_{4s}\tilde{\rho}_0\right]$$

(A.5)

$$A_{31} = \left[\tilde{\rho}_0 u_{so}\left(\frac{dh_0}{h_0 ds} + \frac{d\tilde{\rho}_0}{\tilde{\rho}_0 ds} + \frac{dr}{rds}\right) + A_{3s}\tilde{\rho}_0 - j\Gamma T\tilde{\rho}_0\right]/F_s$$

(A.6)

$$A_{32} = \left(A_{2s}\tilde{\rho}_0 + j\frac{\omega T}{r}\tilde{\rho}_0 u_{so}\right)/F_s$$

(A.7)

$$A_{33} = \frac{1}{\tilde{\rho}_0 F_5} \frac{d\tilde{\rho}_0}{dp} \left[\tilde{\rho}_0 u_{s0} \frac{d\tilde{\rho}_0}{dp} \left(\frac{u_{s0}}{\tilde{\rho}_0^2} \frac{d\tilde{\rho}_0}{ds} + j \frac{\omega T u_{\theta 0}}{\tilde{\rho}_0 r} \right) - j\omega T u_{s0} \tilde{\rho}_0 - A_{4s} \tilde{\rho}_0 \right]$$ (A.8)

$$F_2 = \frac{u_{s0}}{h_0} \left(\frac{d^2 z}{ds^2} - \frac{1}{h_0} \frac{dh_0}{ds} \frac{dz}{ds} \right)$$ (A.9)

$$F_3 = \frac{u_{s0}}{h_0} \left(F_1 - \frac{G_0}{h_0} \frac{dh_0}{ds} \right)$$ (A.10)

$$F_5 = 1 + \frac{u_{s0}^2}{\tilde{\rho}_0} \frac{d\tilde{\rho}_0}{dp}$$ (A.11)

Right hand side definitions for equation 41

$$G_q = \frac{\left(-A_{1s} \tilde{\rho}_0 \frac{dz}{ds} - \tilde{\rho}_0 u_{s0} F_2 - j \tilde{\rho}_0 u_{s0} \frac{\Gamma T}{h_0} \frac{dz}{ds} \right)}{\left(1 - u_{s0}^2 \frac{d\tilde{\rho}_0}{dp} \right)}$$ (A.12)

$$\Gamma = \omega \left(f - u_{\theta 0}/r \right)$$ (A.13)

APPENDIX B

Coefficient definitions for **[B]** *of Eq. (50)*

$$B_{11} = \left[-\tilde{\rho}_0 u_{s0} \left(\frac{dh_0}{h_0 ds} + \frac{d\tilde{\rho}_0}{\tilde{\rho}_0 ds} + \frac{dr}{r ds} \right) - A_{3s}\tilde{\rho}_0 + j\Gamma T\tilde{\rho}_0 \right] u_{s0} / \left(\frac{d\tilde{\rho}_0}{dp} \frac{1}{\tilde{\rho}_0} - u_{s0}\tilde{\rho}_0 \right) + \left(\frac{1}{h_0} \frac{dh_0}{ds} + \frac{1}{\tilde{\rho}_0} \frac{d\tilde{\rho}_0}{ds} + \frac{1}{r} \frac{dr}{ds} \right)$$

(B.1)

$$B_{12} = u_{s0} \left[A_{2s}\tilde{\rho}_0 + j\frac{n\omega T}{r}\tilde{\rho}_0 u_{s0} \right] / \left(\frac{d\tilde{\rho}_0}{dp} \frac{1}{\tilde{\rho}_0} - u_{s0}^2\tilde{\rho}_0 \right)$$

(B.2)

$$B_{13} = \frac{u_{s0}}{\tilde{\rho}_0 F_s} \frac{d\tilde{\rho}_0}{dp} \left[\tilde{\rho}_0 u_{s0} \frac{d\tilde{\rho}_0}{dp} \left(\frac{u_{s0}}{\tilde{\rho}_0^2} \frac{d\tilde{\rho}_0}{ds} + j\frac{n\omega T u_{\theta 0}}{\tilde{\rho}_0 r} \right) - jn\omega T u_{s0}\tilde{\rho}_0 - A_{4s}\tilde{\rho}_0 \right]$$

(B.3)

$$B_{31} = \left[\tilde{\rho}_0 u_{s0} \left(\frac{dh_0}{h_0 ds} + \frac{d\tilde{\rho}_0}{\tilde{\rho}_0 ds} + \frac{dr}{r ds} \right) + A_{3s}\tilde{\rho}_0 - j\Gamma T\tilde{\rho}_0 \right] / F_s$$

(B.4)

$$B_{32} = \left(A_{2s}\tilde{\rho}_0 + j\frac{n\omega T}{r}\tilde{\rho}_0 u_{s0} \right) / F_s$$

(B.5)

$$B_{33} = \frac{1}{\tilde{\rho}_0 F_s} \frac{d\tilde{\rho}_0}{dp} \left[\tilde{\rho}_0 u_{s0} \frac{d\tilde{\rho}_0}{dp} \left(\frac{u_{s0}}{\tilde{\rho}_0^2} \frac{d\tilde{\rho}_0}{ds} + j\frac{n\omega T u_{\theta 0}}{\tilde{\rho}_0 r} \right) - jn\omega T u_{s0}\tilde{\rho}_0 - A_{4s}\tilde{\rho}_0 \right]$$

(B.6)

APPENDIX C

Coefficient definitions for **[C]** *of Eq. (57)*

$$C_{11} = \left[\frac{1}{h_0}\frac{dh}{ds} + \frac{1}{\tilde{\rho}_0}\frac{d\tilde{\rho}_0}{ds} + \frac{A_{3\theta}\omega^2 T^2 f}{rA_{\theta c}} + j\frac{(A_{2\theta}A_{3\theta}\omega T)}{rA_{\theta c}} \right] \tag{C.1}$$

$$C_{21} = A_{3s} - \frac{A_{2\theta}A_{3\theta}A_{2s}}{A_{\theta c}} + j\left(\omega Tf + \frac{A_{3\theta}A_{2s}}{A_{\theta c}} \right) \tag{C.2}$$

$$C_{12} = \frac{\omega T}{A_{\theta c}}\left[\frac{A_{2\theta}bL_s}{r^2 R_i \tilde{\rho}_0} + f\frac{d\tilde{\rho}_0}{dp}A_{4\theta} \right] + j\left[\frac{\Gamma T}{\tilde{\rho}_0}\frac{\tilde{\rho}_0}{dp} + \frac{1}{A_{\theta c}}\left(A_{2\theta}A_{4\theta}\frac{d\tilde{\rho}_0}{dp} - \frac{f\omega^2 T^2 bL_s}{rR_i \tilde{\rho}_0} + \frac{u_0}{\tilde{\rho}_0^2}\frac{d\tilde{\rho}_0}{ds} \right) \right] \tag{C.3}$$

$$C_{22} = -\frac{A_{2\theta}}{A_{\theta c}}\left(A_{4\theta}\frac{d\tilde{\rho}_0}{dp} - \frac{\omega TbL_s}{rR_i \tilde{\rho}_0} \right) - \frac{d\tilde{\rho}_0}{dp}A_{4s} + \frac{j}{A_{\theta c}}\left(A_{2\theta}\frac{b}{r}\frac{L_s}{R_i \tilde{\rho}_0} + \frac{d\tilde{\rho}_0}{dp}\omega TfA_{4\theta} \right) \tag{C.4}$$

$$A_{\theta c} = A_{2\theta}^2 + \omega^2 T^2 f^2 \tag{C.5}$$

APPENDIX D

Coefficient definitions for **[D]** *of Eq. (60)*

$$D_{11} = \left[\frac{1}{h_0}\frac{dh}{ds} + \frac{1}{r}\frac{dr}{ds} + \frac{A_{3\theta}n^2\omega^2 T^2 f}{rA_{\theta c}} + j\frac{(A_{2\theta}A_{3\theta}n\omega T)}{rA_{\theta c}}\right] \tag{D.1}$$

$$D_{21} = A_{3s} - \frac{A_{2\theta}A_{3\theta}A_{2s}}{A_{\theta c}} + j\left(n\omega Tf + \frac{A_{3\theta}A_{2s}}{A_{\theta c}}\right) \tag{D.2}$$

$$D_{12} = \frac{n\omega T}{A_{\theta c}}\left[\frac{A_{2\theta}bL_s}{r^2 R_i \tilde{\rho}_0} + f\frac{d\tilde{\rho}_0}{dp}A_{4\theta}\right] + j\left[\frac{\Gamma T}{\tilde{\rho}_0}\frac{d\tilde{\rho}_0}{dp} + \frac{1}{A_{\theta c}}\left(A_{2\theta}A_{4\theta}\frac{d\tilde{\rho}_0}{dp} - \frac{fn^2\omega^2 T^2 bL_s}{rR_i \tilde{\rho}_0}\right)\right] \tag{D.3}$$

$$D_{22} = -\frac{A_{2\theta}}{A_{\theta c}}\left(A_{4\theta}\frac{d\tilde{\rho}_0}{dp} - \frac{n\omega TbL_s}{rR_i \tilde{\rho}_0}\right) - \frac{d\tilde{\rho}_0}{dp}A_{4s} + \frac{j}{A_{\theta c}}\left(A_{2\theta}\frac{b}{r}\frac{L_s}{R_i \tilde{\rho}_0} + \frac{d\tilde{\rho}_0}{dp}n\omega TfA_{4\theta}\right) \tag{D.4}$$

$$A_{\theta c} = A_{2\theta}^2 + n^2\omega^2 T^2 f^2 \tag{D.5}$$